SEARCH FOR SUPERSYMMETRY IN A THREE LEPTON

PLUS JETS SIGNATURE

Approved by:

_____

Dr. Robert Kehoe

_____

Dr. Kent Hornbostel

_____

Prof. Ryszard Stroynowski

_____

Dr. Vladimir Ajaev

SEARCH FOR SUPERSYMMETRY IN A THREE LEPTON

PLUS JETS SIGNATURE

A Dissertation Presented to the Graduate Faculty of the

Dedman College

Southern Methodist University

in

Partial Fulfillment of the Requirements

for the degree of

Doctor of Philosophy

with a

Major in Physics

by

Pavel Zarzhitsky

(M.S., Byelorussian State University, 1992)

July 31, 2008

ACKNOWLEDGMENTS

I would like to express my gratitude to my advisor Robert Kehoe. I would not be able to finish the thesis without his help. I would like to thank to everyone at Physics Department of SMU for their support during years of my graduate study.

Zarzhitsky , Pavel   M.S., Byelorussian State University, 1992

Search for Supersymmetry in a Three Lepton

Plus Jets Signature

Advisor: Professor Robert Kehoe

Doctor of Philosophy degree conferred July 31, 2008

Dissertation completed July 31, 2008

We present a search for three lepton plus jets supersymmetric signal at ATLAS detector, LHC, at $\sqrt{s} = 14$ TeV. The signal signature must contain three isolated leptons with p_T's above 5 GeV and two jets with p_T's above 40 GeV. The leptons must form a same flavor opposite charge pair. The analysis was done using the Monte Carlo data equivalent to 1 fb^{-1} of the real data. $t\bar{t}$, WZ, $Zb\bar{b}$ and Z+jets processes were considered as backgrounds. The signal extraction from the backgrounds was done using optimization cuts in five variables: p_T's of leptons, H_T and $\not{E}_T$. It was shown that the statistical significance $\rho = \frac{S}{\sqrt{S+B}} = 6.3$ for 1 fb^{-1}. This allows an early SUSY discovery. The discovery limit $\rho = 5$ can be reached at 650 pb^{-1}. The effect of main jet calibration uncertainty determined to be small.

TABLE OF CONTENTS

LIST OF FIGURES

LIST OF TABLES

xiii

This dissertation is dedicated to my wife Larisa.

Chapter 1

INTRODUCTION

The word physics was first mentioned by Aristotle in his famous work "Physics"(or "Physica", or "Physicae Auscultationes" meaning "lessons"). The book is a collection of lessons about theoretical, methodological and philosophical concerns, rather than physical theories or contents of particular investigations. Aristotle tried to provide a complete description of the universe and its laws although his approach was not based on any real experiments. Being very popular in Medieval times, the book finally give the name to modern physics: part of science that investigates the behavior of matter, energy and fundamental forces.

Since the time of the ancient Greeks people have been wondering what matter consists of. The first theory with experimental approval was atomic theory. According to it, everything consisted of combinations of several different kinds of atoms (or indivisible units). Experiments held by Dalton and Avogadro provided the atomic theory a steady experimental support and it was accepted by most scientists by the beginning of the 19th century. In 1869, Mendeleev presented his periodic table. The table classified atoms by their properties and predicted several unknown elements that were found later.

The discoveries of the electron by Thompson and the nucleus by Rutherford showed that atoms are complicated objects with internal structure. So the atom consisted of the nucleus and electrons that were held together by an electromagnetic interaction. Soon protons and neutrons were discovered as parts of the atomic nucleus and a new "strong" interaction was introduced in nature to bind them together.

With time more and more elementary particles were discovered. Many of the heavy particles decayed into lighter ones. For example, β decay is a decay of a neutron into a proton, electron and anti-neutrino. A "weak" interaction had to be introduced to explain these decays. Investigating patterns in the properties of elementary particles allowed to classify them in different groups in a way somewhat similar to the periodic table for atoms. This finally resulted in a discovery of their internal structure.

Particle physics began in the 1930s as a branch of physics that investigated elementary particles and their interactions. At this time Yukawa suggested the first model of strong interactions [1]. He suggested that protons and neutrons are attracted to each other because of the interchange of massive scalar particles - "pions" (π). The mass of the pion explained why the strong interaction has a short range. At the same time Fermi proposed a very successful model of β-decay that was the first model of weak interactions [2]. In the model, four particles (neutron, proton, electron and anti-neutrino) directly interact with each other (so called contact interaction) and the strength of the interaction is described by the Fermi constant, G_F. The major breakthrough happened in 1940s when Feynman, Dyson, Schwinger, and Tomonaga were able to provide a successful perturbation theory of the electromagnetic interactions - quantum electrodynamics (QED) [3], [4]. This model became an example for most of the later particle physics models. In 1970s Weinberg and Salam joined together weak and electromagnetic interactions, assuming that there is a hidden symmetry that connects them together [5]. The hypothesis of quarks and color charges developed in 1963-65 (see next section) was the beginning of the modern theory of the strong interaction - Quantum Chromodynamics (QCD). At the present time there is no satisfactory quantum theory of gravity. The theory that is used now is sometimes called the Standard Model (SM). It groups electroweak theory with QCD and provides a good description of known experimental results.

1.1. Current theory.

Table 1.1.   Standard Model fermions

	Leptons			Quarks		
	flavor	mass	charge	flavor	mass	charge
The 1st generation	e	0.0005 GeV	-1	u	0.003 GeV	+2/3
	ν_e	$< 10^{-8}$ GeV	0	d	0.006 GeV	-1/3
The 2nd generation	μ	0.106 GeV	-1	c	1.3 GeV	+2/3
	ν_μ	$< 10^{-4}$ GeV	0	s	0.1 GeV	-1/3
The 3d generation	τ	1.777 GeV	-1	t	171 GeV	+2/3
	ν_τ	< 0.02 GeV	0	b	4.3 GeV	-1/3

Table 1.2.   Standard Model bosons

Interaction	boson	mass	charge	spin	relative strength	range, m
strong	gluon	0	0	1	1	10^{-18}
electromagnetic	photon	0	0	1	0.01	∞
weak	$W^\pm$	80 GeV	± 1	1	10^{-13}	10^{-14}
	Z^0	91 GeV	0	1		
gravity	graviton	0	0	2	10^{-38}	∞

According to the Standard Model matter consists of spin 1/2 particles, fermions following Fermi statistics. They are listed in Table 1.1. Bosons (Table 1.2), integer spin particles, are carriers of the fundamental interactions. There are four fundamental interactions: strong, electromagnetic, weak and gravity. Each of these interactions is characterized by a coupling constant, a number determining the strength of the interaction.

The Standard Model is a quantum field theory. It is based on the principle of least action. The principle of the action states that when a system evolves from one state to another between times t_1 and t_2, it goes through the "path" in configuration space that leaves action at extremum (usually minimum). The action is

$$S = \int L d^4 x, \tag{1.1}$$

where L is a Lagrangian of the system. The physical meaning of the Lagrangian is a difference between kinetic and potential energy of the system. If action is at extremum, then

$$\delta S = \delta(\int L d^4 x) = 0. \tag{1.2}$$

The interactions between fermions are describes through "local gauge" theories. These theories imply that the Lagrangian is invariant under gauge transformation, even if the transformation law depends on the position. The transformation that leaves the Lagrangian unchanged represents a symmetry and is associated with the conserved charge and current according to the Noether's theorem. An example of the conserved charge is an electric charge in QED. The most general symmetry group in the SM is $SU(3) \times SU(2) \times U(1)$. The $SU(2) \times U(1)$ group describes electroweak interactions and corresponds to the conservation of the hypercharge and weak isospin. The $SU(3)$ group describes strong interaction and corresponds to the conservation of 3 color charges.

1.1.1. Electroweak Theory.

Weinberg and Salam created a unified theory of weak and electromagnetic inter-

actions [5]. The SU(2) group is related to the conservation of weak isospin, T, and is associated with 3 vector bosons $W^{1,2,3}$ (see [8], [7] for detailed description). The U(1) group is related to the conservation of the hypercharge Y that can be found from:

$$Q = T^3 + \frac{Y}{2},\tag{1.3}$$

where Q is electromagnetic charge, T^3 is the third component of the isospin. The U(1) group has one vector boson B_0. In the experiments we observe mass eigenstates of bosons that can be obtained by mixing gauge eigenstates $W^{1,2,3}$ and B_0:

$$W^\pm = \frac{1}{\sqrt{2}}(W^1 \mp iW^2)\tag{1.4}$$

$$\gamma = B_0 \cos\theta_W + W^3 \sin\theta_W\tag{1.5}$$

$$Z = -B_0 \sin\theta_W + W^3 \cos\theta_W,\tag{1.6}$$

where θ_W is a weak mixing angle. Here, $W^\pm$ and Z are massive weak bosons and γ is a massless photon.

The SU(2) interaction is coupled only to the left-handed fermions, so right- and left-handed components of the fermion fields interact differently. Left-handed fermions form a doublet under the weak interaction, while right-handed fermions make a singlet. For example, the electron field can be represented:

$$e \to \begin{pmatrix} e_L \\ \nu_e \end{pmatrix} e_R\tag{1.7}$$

The coupling constants of the SU(2) and U(1) groups are g and $\frac{1}{2}g'$. Their relation to the electromagnetic constant e is given by

5
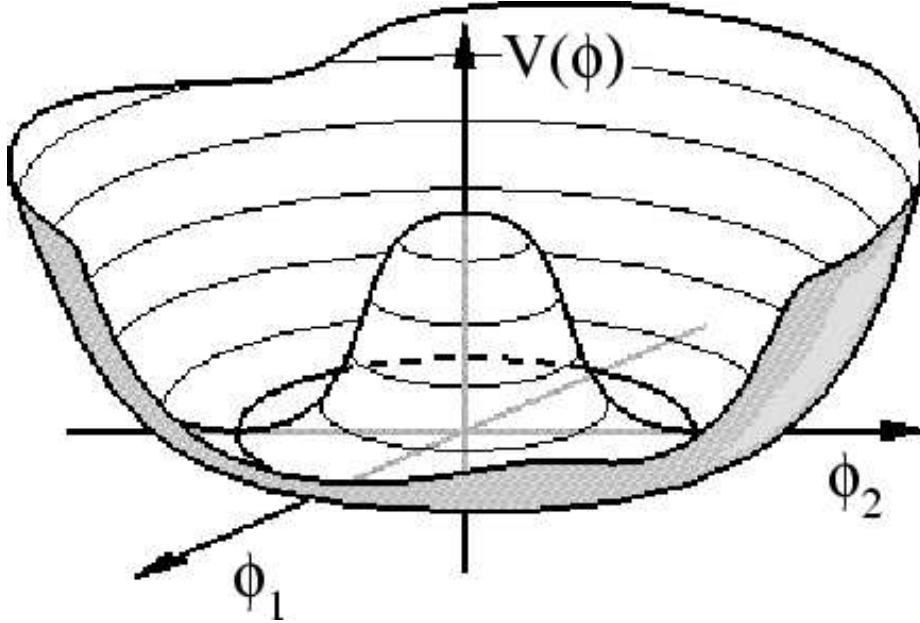
Figure 1.1. "Mexican hat" potential for the Higgs field.

$$g \sin \theta_W = g' \cos \theta_W = e, \qquad (1.8)$$

Theoretically, all electroweak bosons must be massless, but we know from observation that the range of the weak interactions is small, so at least some of them should have mass. The mass is generated by a Higgs boson through the mechanism of spontaneous symmetry breaking [6]. The spontaneous symmetry breaking is provided by the shape of the Higgs field potential.

The Lagrangian of the Higgs field is [8],[7]

$$L = (\partial \phi_\mu)^\dagger \partial \phi_\mu - \mu^2 \phi^\dagger \phi - \lambda (\phi^\dagger \phi)^2, \qquad (1.9)$$

where ϕ is a Higgs field, the first term is a standard kinetic energy term, and last two terms are potential energy. λ and μ^2 are constants describing the potential. If

$\mu^2 < 0$ and $\lambda > 0$, then the potential has the "sombrero" shape shown on the Figure 1.1. The minimum of the potential is given by

$$\phi^\dagger \phi = -\frac{\mu^2}{2\lambda} \tag{1.10}$$

The Higgs field is a complex scalar field, so it can be considered as a combination of two real scalar fields, ϕ_1 and ϕ_2

$$\phi = \phi_1 + i\phi_2. \tag{1.11}$$

The minimum of the potential is

$$\phi^\dagger \phi = \frac{1}{2}(\phi_1^2 + \phi_2^2) = -\frac{v^2}{2} \tag{1.12}$$

where $v = -\mu^2/\lambda$ is a vacuum expectation value of the Higgs field. The Lagrangian is invariant under the $SU(2) \times U(1)$ symmetry transformation, but the ground state can occur on any point of the minimum circle given by Eq. 1.12. The position of the ground state is unpredictable. The point, chosen by nature provides a "spontaneous symmetry breaking", because after the ground state is selected, all directions are no longer equivalent.

For simplicity, we can choose ground state to be in ϕ_1 direction. Then the Higgs field will look like

$$\phi(x) = \begin{pmatrix} 0 \\ \frac{v+h(x)}{\sqrt{2}} \end{pmatrix}, \tag{1.13}$$

where $h(x)$ is a real field. Higgs field is expanded around the ground state.

The general term that generates the mass of the particle in the Lagrangian has form $\frac{1}{2}m^2\psi^\dagger\psi$. If we substitute expression 1.13 in the Lagrangian, it can be shown that the Higgs mass is [8]

$$m_H = \sqrt{2\lambda v^2}. \tag{1.14}$$

The masses of the gauge bosons are also generated by the Higgs field. When we substitute the Higgs field in the electroweak Lagrangian and find the terms that have the form of the mass term, then [8]

$$M_W = \frac{1}{2}vg \tag{1.15}$$

$$M_Z = \frac{1}{2}v\sqrt{g^2 + g'^2} \tag{1.16}$$

$$M_\gamma = 0 \tag{1.17}$$

where g and g' are weak couplings. Thus, four massless gauge vector bosons from the $SU(2) \times U(1)$ group are mixed, providing three massive weak bosons and a massless photon.

The situation is more complicated for the fermions. The mass terms like $-m_\psi^2 \bar{\psi}\psi$ are excluded by gauge invariance. If we couple the Higgs field to a fermion field, for example the electron, we obtain the following terms in the Lagrangian [8]:

$$L_{H-e} = -\frac{G_e}{\sqrt{2}}v(\bar{e}_L e_R + \bar{e}_R e_L) - \frac{G_e}{\sqrt{2}}(\bar{e}_L e_R + \bar{e}_R e_L)h \tag{1.18}$$

We choose G_e such that

$$m_e = \frac{G_e}{\sqrt{2}}v \tag{1.19}$$

and get the required mass term $m_e \bar{e} e$ in the Lagrangian:

$$L_{H-e} = -m_e \bar{e} e - \frac{m_e}{v} \bar{e} e h. \tag{1.20}$$

It should be mentioned though the fermion mass term was found, the value of the mass was not predicted by theory. The constant G_e has no theoretical restrictions so far and can be found only experimentally through measuring electron mass.

So, the Weinberg and Salam theory joined together electromagnetic and weak interactions into an electroweak interaction characterized by the symmetry group $SU(2) \times U(1)$. This symmetry happens to be broken through the spontaneous symmetry breaking mechanism, because the ground state of the Higgs field is not symmetric. Symmetry breaking provides mass for three out of four electroweak bosons and as well as for the fermions.

1.1.2. Quantum Chromodynamics

The interaction between quarks and gluons is described by the strong force that has a gauge group $SU(3)$. The $SU(3)$ group corresponds to the conservation of three "color" charges for an interaction mediated by eight vector bosons (gluons). Color charge can have three values red, green, or blue, where the names of the colors are arbitrary. Anti-quarks have anti-colors: anti-red, anti-green, or anti-blue. Gluons carry eight possible color-anti-color combinations. The quantum theory of the strong interaction is called quantum chromodynamics (QCD). The largest difference of QCD from QED is the fact that gluons also carry color charge. This means, that unlike photons, gluons may interact with each other without any quarks.

At short distances strong coupling constant is sufficiently small and allows to perform perturbative calculations. This property is called asymptotic freedom. The

interaction between two quarks grows with distance. It is believed that the potential is proportional to the distance in the absence of the light quarks (u and d).

Another property of QCD: color confinement. We cannot observe isolated colored particles. Experimentally, we only observe white or colorless objects. There are three ways to have colorless object. The first one is a combination of gluons termed a "glueball". They are not found experimentally, but glueballs are believed to be heavy and unstable, so their observation is difficult. The other combination is quark-anti-quark with, for example, red-anti-red colors. These combinations are called mesons, for example $\pi^{0,\pm}$. The last combination is a combination of three quarks with red, green and blue colors. These combinations are called baryons, for instance the proton or neutron.

Individual quark can not be removed from the baryon or meson. If we try to separate quark-anti-quark pair, then the interaction energy grows with distance. Finally, the energy becomes large enough to produce a quark-anti-quark pair out of the vacuum. The new quark is attracted to the initial anti-quark, the new anti-quark is attracted to the initial quark. So, instead of creating a free quark, we just create new colorless hadrons from the vacuum. This process is called hadronisation or fragmentation.

The hadronisation process can not be calculated using perturbative theory, but there are several phenomenological model that are used. In the Field-Feynman model [9] the production of colorless objects is treated as a process local to the high energy quark. Each quark-anti-quark pair is produced independently from the others, leaving the initial quark with lower momentum. In the cluster fragmentation model the jet is formed through perturbatively calculated gluons that split in $q\bar{q}$ or diquark-antidiquark $D\bar{D}$ pairs. These pairs are combined to clusters that can be mesonic $q\bar{q}$, $D\bar{D}$ or baryonic qD, $\bar{q}\bar{D}$. The clusters decay either to lower mass clusters or to

hadrons. In the string fragmentation model [9], two quarks are connected to each other by a narrow tube or "string" of the strong color force lines. The particles oscillate at the ends of the string until a $q\bar{q}$ is created along the string. The new quarks cut the string creating two shorter ones. The quarks at the end of the new strings also oscillate and might create another $q\bar{q}$ pair if they have enough energy.

1.1.3. Grand Unification.
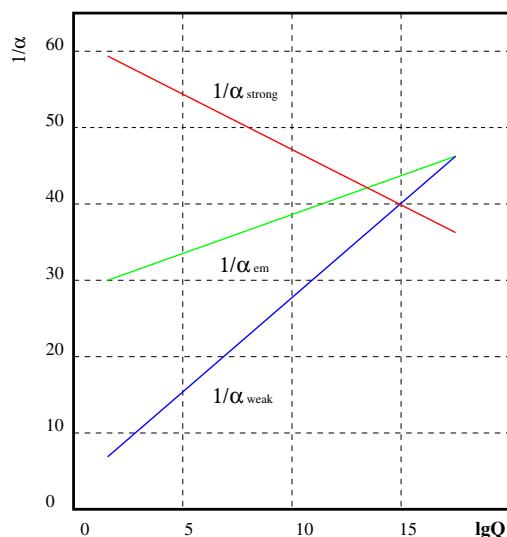
Figure 1.2. The behavior of the coupling constants at different energy scales.

Did electroweak theory really unify electromagnetic and weak interactions? The answer is not so obvious. The symmetry group $SU(2) \times U(1)$ is a combination of two disconnected sets of gauge transformations from $SU(2)$ and $U(1)$. They have different coupling constants g and g' and their ratio need to be measured experimentally. The true unification is possible only if both $SU(2)$ and $U(1)$ are subsets of a larger group G, where g and g' are somehow connected.

11

Let us suppose that there is a group G that has $SU(3) \times SU(2) \times U(1)$ as a subgroup. This group would unify strong and electroweak interactions, its transformations should relate electroweak couplings g and g' to each other and to the strong coupling g_s. All interactions should be described by a new coupling g_G related to all previous couplings.

In general, the coupling constant depends on the energy of the interaction. Experimentally we see a coupling that is a sum of the bare coupling (that is in the Lagrangian) and contribution from different loops. This effect is called "running coupling constant". The higher the energy, the more loops are essential. The behavior of the couplings is shown at Figure 1.2 [8]. The energy range where they all meet is called the unification scale and 10^{16} GeV. The energy scale where gravitational effects are important is called the "Planck scale", 10^{18} GeV.

1.2. Problems of the Standard Model.

Partly because of the near convergence of g_i at 10^{16} GeV people search for the SM extensions. We know that a new model is required at the Planck scale, $M_P \sim 10^{18}$ GeV, because there is no quantum field theory of the gravity. Assuming unification holds something new must exist at the intermediate scale between the weak energy scale M_W and the Planck scale M_P.

1.2.1. Hierarchy problem.

The Standard Model requires a non-vanishing vacuum expectation value for H at the minimum of the potential. From the properties of the weak interaction we know that $\langle H \rangle$ is approximately 174 GeV [15], so m_H^2 must be an order of $(100 GeV)^2$. The correction to the Higgs mass is
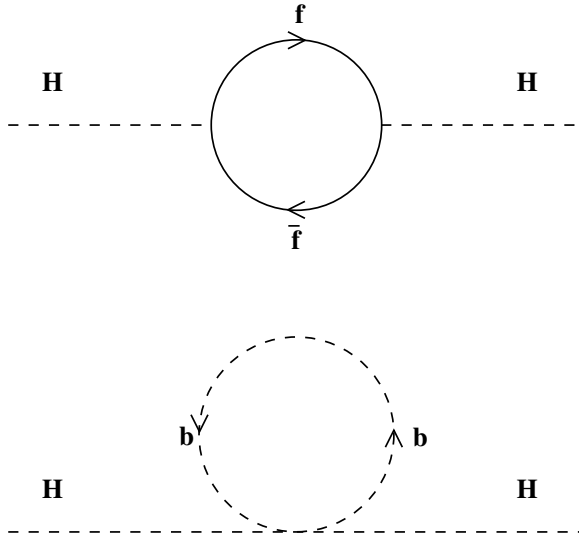
Figure 1.3. Contributions to the Higgs mass from fermion and boson loops

$$\triangle m_H^2 = -\frac{|\lambda_f|^2}{8\pi^2}\Lambda_{UV}^2 + \frac{\lambda_S}{16\pi^2}[\Lambda_{UV}^2 - m_S^2 ln(\Lambda_{UV}/m_S)] \qquad (1.21)$$

The first term come from the fermion loop and the second is from the boson. Λ_{UV} is an ultraviolet momentum cutoff. If we want to get a finite result using perturbation theory it must be a large number. The natural choice for Λ_{UV} is to be at the Planck scale. The problem is that the Higgs field is coupled to every fundamental particle, so we must get $(100 \text{ GeV})^2$ for m_H^2 by canceling terms that are $(10^{18})^2$. Thus an extremely precise cancellation of non-related terms is required to get a reasonable result.

1.3. Cosmology.

13

Surprisingly, the particle physics dealing with the smallest effects of the nature is connected to cosmology, the field of physics related to the largest objects in the Universe. The connection goes through the evolution of the Universe. At early times, just after Big Bang, the Universe was very hot and allowing very heavy particles to exist. Thus, we can get some information about the energy scale far beyond out ability to reach experimentally by studying cosmological models. The Universe we have now depends on its evolution at early times.

One of the important questions is if out Universe finite or infinite or, in other words, if it is flat or non-flat. This question has direct relation to particle physics. If the Universe is flat, its matter-energy density must be sufficiently large. Mass-energy density is usually referred as $\Omega = \Omega_m + \Omega_\lambda$, where Ω_m is a matter density, Ω_λ is an energy density. Ω is a fraction of the amount required for a flat universe. So, if $\Omega > 1$, the universe is flat, if $\Omega < 1$ the universe is non-flat.

According to the recent cosmological experiments, including red-shift measurements from distant supernovae [11] and precision measurements of the Cosmic Microwave Background (CMB) by the Wilkinson Microwave Anisotropy Probe (WMAP) [10] the $\Omega = 1$. At the same time WMAP results show that the matter density, Ω_m, is approximately ten times larger than observable baryonic mass density (the objects that emit light, like stars). Dark matter is matter that can not be observed via normal astrophysics techniques. It can exist in two forms: dark baryonic matter in form of dead stars or massive planets or weakly interacting elementary particles. Searches for baryonic dark matter showed that it cannot provide a substantial part of dark matter.

Weakly interacting elementary particles can be divided into three groups: cold dark mater, hot dark matter and axions. Particles that were in thermal equilib-

rium with the universe in the early stage will fall out the equilibrium with time the decoupling time or temperature depends on the rate of the universe expansion and coupling constant of these particles to the others. Particles that are non-relativistic by the time when galaxies start to form are called "cold dark matter", particles that remain relativistic at this time called "hot dark matter". The simplest example of both hot and cold dark matter is a neutrino. A heavy neutrino (100 GeV) is cold dark matter, while light one (< 20 eV) is hot dark matter. The third group can arise from QCD during the phase transition as the universe cools down. In this case the result can be a gas of axions that might provide a substantial part of the dark matter.

All these consideration give an important tool for particle physics. A possible dark matter candidate, that appears in any theoretical model, provides it an extra points. Due to the astrophysical reasons the cold dark matter is strongly favored. One of the possible cold dark matter candidates is given by supersymmetry (lightest supersymmetric particle). LHC will provide an opportunity to test many dark matter candidates.

Chapter 2

THE THEORY OF SUPERSYMMETRY

2.1. The Basic Idea.

Supersymmetry or SUSY is one of the most powerful extensions of SM. It is based on an assumption that there is one more symmetry in nature that relates fermions and bosons. The new symmetry is called supersymmetry [13],[14].

If the supersymmetry exists we should have at least double the number of fundamental particles by providing a superpartner with the same properties, but different spin statistics, to each known particle. The masses of the supersymmetric particles must be higher than our experimental energy limit, otherwise we would detect them already. Since the masses of the superpartners are different then masses of normal particles, supersymmetry must be broken.

Supersymmetry allows to solve some of the Standard Model problems listed in the previous chapter.

- Supersymmetry provides a new physics that lies between weak and Planck energy scales.

- In supersymmetric models running couplings can be arranged to meet at the same point.

- The hierarchy problem is solved in a very natural way. We do not need fine tuning to get a small Higgs mass. All fermions and bosons form pairs. The

contributions from superpartners are the same and cancel each other, because fermions and bosons loops contribute to the mass term with different signs.

- In many SUSY models, the lightest supersymmetric particle (LSP) is stable and if neutral it provides an excellent dark matter candidate.

All these reasons make a SUSY search one of the most important tasks for the LHC. Most of the beyond SM models, including SUSY, have one of their Higgs bosons in the SM range. A Higgs discovery at LHC would not tell us immediately if SM is a final theory or what is the physics beyond it. That is why direct SUSY searches are important to prove or eliminate supersymmetry. The following discussion is based mostly on review [15].

The superpartners for all SM particles are listed in Tables 2.1 and 2.2. To make a name for the superpartner " should be prefixed to the particle name for fermions. For example the superpartner of the electron is called selectron. For the superpartners of bosons, " should be suffixed to the particle name. For instance a gluon will have a superpartner gluino.

Table 2.1. Supersymmetric partners of the fermions

flavor	name	spin	flavor	name	spin
e	electron	1/2	$\tilde{e}_L\ \tilde{e}_R$	selectron	0
ν_e	neutrino	1/2	$\tilde{\nu}_e$	sneutrino	0
μ	muon	1/2	$\tilde{\mu}_L\ \tilde{\mu}_R$	smuon	0
ν_μ	neutrino	1/2	$\tilde{\nu}_\mu$	sneutrino	0
τ	τ lepton	1/2	$\tilde{\tau}_L\ \tilde{\tau}_R$	stau	0
ν_τ	neutrino	1/2	$\tilde{\nu}_\tau$	sneutrino	0
q	quark	1/2	$\tilde{q}$	squark	0

17

Table 2.2. Supersymmetric partners of the bosons

boson	name	spin	SUSY partner	name	spin
B^0	B boson	1	$\tilde{B}^0$	bino	1/2
$W^{1,2,3}$	W boson	1	$\tilde{W}^{1,2,3}$	wino	1/2
g	gluon	1	$\tilde{g}$	gluino	1/2

The Higgs sector of SUSY is more complicated. In order to avoid gauge anomalies, we need two Higgs fields H_u and H_d They both are complex scalar field doublets, having one neutral and one charged component: $(H_u^+, \ H_u^0)$ and $(H_d^0, \ H_d^-)$. The superpartner of the Higgs bosons are four higgsinos with spin 1/2. Two of them are neutral, one is positive and one is negative.

At the experiment mass eigenstates are detected. The gauge bosons superpartners (also called gauginos) are mixed in a similar way that the $W-$ and $B-$ bosons mixed to give $W^\pm$, Z^0 and γ. Mixing of two neutral gauginos and two neutral higgsinos produces four mass eigenstate neutralinos ($\tilde{\chi}_{1,2,3,4}^0$), while mixing of the charged gauginos and charged higgsinos gives four charginos ($\tilde{\chi}_{1,2}^-$, $\tilde{\chi}_{1,2}^+$).

2.2. Minimal Supersymmetric Model

Let us consider Minimal Supersymmetric Model (MSSM) as an example of the simplest supersymmetric theory. MSSM is a supersymmetric extension of Standard Model with minimal changes. The Lagrangian of the MSSM should be invariant under the supersymmetric transformation. Using this invariance condition and some general properties of a renormalizable supersymmetric field theory the general form of the Lagrangian can be found, [15], [16]. The Lagrangian must have the same number of fermion and boson fields (corresponding to partner-superpartner pairs). It

should also contain extra fields that are called auxiliary. Auxiliary fields are used to keep supersymmetry algebra closed off-shell and have no real particle associated with them, see [15], [16].

The interactions and masses of all particles are determined by their gauge transformation properties and by the superpotential W_{SS}. For MSSM the superpotential is, [15]

$$W_{MSSM} = \bar{u} y_u Q H_u - \bar{d} y_d Q H_d - \bar{e} y_e L H_d + \mu H_u H_d. \tag{2.1}$$

The objects $H_u, H_d, Q, \bar{u}, \bar{d}, L, \bar{e}$ are chiral superfields corresponding to the chiral supermultiplets of Higgs and higgsinos, quarks and squarks, leptons and sleptons. Fields corresponding to the superpartners can be grouped together with the corresponding auxiliary fields and form a supermultiplet that is called a superfield. A superfield must contain bosonic, fermionic and auxiliary components. By construction, the superpotential had to be an analytic function of chiral superfields, so terms like $H_u^* H_u$ or $H_d^* H_d$ are forbidden. y_u, y_d, y_e are dimensionless Yukawa coupling parameters (3×3 matrices in family space). The μ term provides masses for MSSM Higgses and contributes to the higgsino masses. It does not contribute to the electroweak symmetry breaking mechanism.

The third generation fermions (t, b and τ) are much heavier than other fermions. That is why Yukawa couplings are important only for the third generation, and Yukawa matrices can be approximated like

$$y_u \approx \begin{pmatrix} 0 & 0 & 0 \\ 0 & 0 & 0 \\ 0 & 0 & y_t \end{pmatrix},$$

$$y_d \approx \begin{pmatrix} 0 & 0 & 0 \\ 0 & 0 & 0 \\ 0 & 0 & y_b \end{pmatrix},$$

$$y_e \approx \begin{pmatrix} 0 & 0 & 0 \\ 0 & 0 & 0 \\ 0 & 0 & y_\tau \end{pmatrix}$$
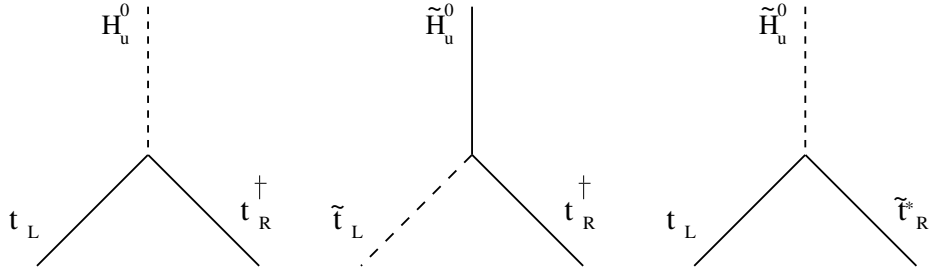
Figure 2.1. The top-quark Yukawa coupling.

In this limit only t, b and τ are coupled to the Higgs fields through Yukawa couplings. The corresponding interaction vertexes are given on Figure 2.1. The potential is

$$W_{MSSM} \approx y_t(\bar{t}tH_u^0 - \bar{t}bH_u^+) - y_b(\bar{b}tH_d^- - \bar{b}bH_d^0) - y_\tau(\bar{\tau}\nu_\tau H_d^- - \bar{\tau}\tau H_d^0) + \mu(H_u^+ H_d^- - H_u^0 H_d^0).$$

$$(2.2)$$

The terms $y_t\bar{t}tH_u^0$, $y_b\bar{b}bH_d^0$, $y_\tau\bar{\tau}\tau H_d^0$ provides masses for top, bottom and τ. Other terms describe different interactions of Higgs-higgsino and third generation fermions-sfermions.
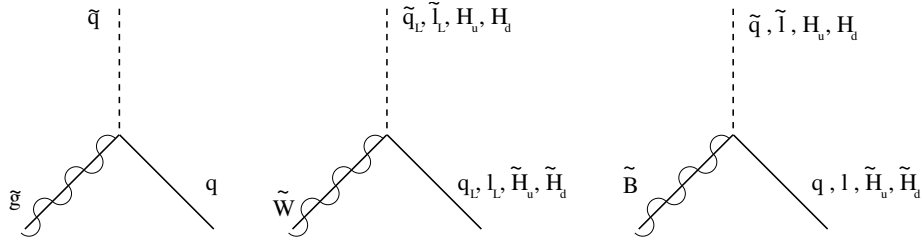
Figure 2.2. Couplings of the gluino, wino and bino to MSSM.

Production and decay of the supersymmetric particles is usually dominated by the interactions of the gauge-coupling strength. These interactions are large enough for all generations, not only for the third one.
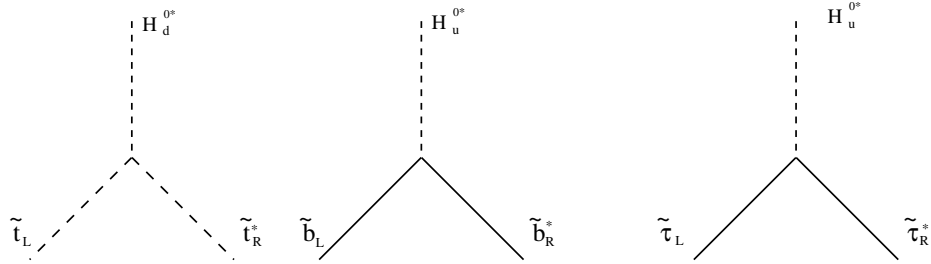
Figure 2.3. Some of the supersymmetric scalar couplings.

The gluino, wino and bino couple to (squark, quark), (slepton, lepton) and (Higgs, higgsino) pairs. These interactions have gauge coupling with g and g' strength. Their vertexes are shown on the Figure 2.2. The μ-term and Yukawa couplings combine to provide interactions between three scalars. The corresponding Feynman diagrams are shown in Figure 2.3.

The MSSM model is defined by the set of parameters:

- m_0: universal scalar mass.

- $m_{1/2}$: universal gaugino mass.

- A_0: universal trilinear coupling.

- $\tan\beta$: ratio of vacuum expectation value for the SUSY Higgses.

- $sgn(\mu)$:

2.3. R-parity

In the Standard Model baryon and lepton numbers are conserved. Baryon number $B=+1/3$ for Q_i; $B=-1/3$ for $\bar{u}_i$, $\bar{d}_i$; and $B=0$ for all others. The total lepton number $L=+1$ for L_i; $L=-1$ for $\bar{e}_i$; and $L=0$ for all others. In general, that is not true for supersymmetry. The superpotential of the MSSM is not the most general form of the superpotential. The most general superpotential can contain terms like, [15], [16]:

$$W_{L=1} = \frac{1}{2}\lambda^{ijk}L_iL_j\bar{e}_k + \lambda'^{ijk}L_iQ_j\bar{d}_k + \mu'^i L_i H_u \qquad (2.3)$$

$$W_{B=1} = \frac{1}{2}\lambda''^{ijk}\bar{u}_i\bar{d}_j\bar{d}_k, \qquad (2.4)$$

where i,j,k are family indexes. So, these terms should violate baryon or lepton number by 1. There is no experimental results that indicate B or L violation. It is possible to postulate L and B conservation laws in supersymmetry, but it is more elegant to introduce a new symmetry that can eliminate B and L changing terms from Lagrangian. This new symmetry is called "R-parity" or "matter parity".

R-parity is a new quantum number that is defined as

$$R = (-1)^{3B+L+2S,} \qquad (2.5)$$

22

$R = +1$ for all conventional particles and $R = -1$ for their superpartners. R-parity may not be conserved. In SUSY model where it is conserved there are several phenomenological consequences:

- The lightest supersymmetric particle (LSP) is stable and it is a very attractive dark matter candidate if is electrically neutral.

- The decay products of all sparticles must have an odd number of LSP's

- Supersymmetric particles must be produced in pairs in accelerator.

2.4. SUSY Breaking

Any realistic model should include supersymmetry breaking. The symmetry breaking can be either explicit, when the symmetry breaking terms are added to the Lagrangian, or spontaneous, when the Lagrangian remains symmetric, but the vacuum expectation value is not 0 (similar to Higgs mechanism in electroweak theory). From a theoretical point of view, we expect to have a spontaneous breaking mechanism.

The vacuum expectation is

$$\langle 0|H|0\rangle = \langle 0|V|0\rangle \tag{2.6}$$

where H is a Hamiltonian and V is a scalar potential. Therefore supersymmetry is not broken if auxiliary fields F_i (for chiral supermultiplets) and D^α (for gauge supermultiplets) do not vanish simultaneously in the ground state. The breaking mechanism can go through the D-term [17] or through the F-term [18]. D-term supersymmetry breaking theory has difficulty in explaining MSSM particle masses [15]. The other possibility is F-term SUSY breaking (O'Raifeartaigh) model.

$$F_i = \frac{\delta W}{\delta \phi^i}, \tag{2.7}$$

so if we can choose superpotential W in such a way that equations $F_i = 0$ do not have simultaneous solutions, then $V = \sum_i |F_i|^2$ will have to be positive at its minimum and supersymmetry is broken.

The supersymmetry-breaking parameter cannot belong to the MSSM. In the case of a D-term we cannot get acceptable masses, in case of an F-term none of the MSSM singlets can generate non 0 vacuum expectation. So, to explain SUSY breaking we must extend MSSM and there are two main approaches to this extension.

In gauge-mediated supersymmetry breaking (GMSB) models, the soft supersymmetry breaking terms generated by the ordinary gauge interactions. The basic idea is to introduce some new chiral supermultiplets, called messengers, that couple to the ultimate source of the SUSY breaking and also coupled indirectly to the MSSM particle through the ordinary gauge bosons.

In the gravity mediated supersymmetry breaking models super gravity (SUGRA) or minimal supergravity (mSUGRA) the MSSM and spontaneous symmetry-breaking sector are connected through the gravitational interaction. In this case, the partner of the graviton (gravitino) obtains mass in the same way as W and Z bosons obtain mass in the Standard Model. This model is important in cosmology, because the large mass of the gravitino contributes to the density of the universe.

2.5. SUSY Production and Decays at LHC

At hadron colliders sparticles can be produced through electroweak processes:

$$q\bar{q} \to \tilde{\chi}_i^+ \tilde{\chi}_j^-, \ q\bar{q} \to \tilde{\chi}_i^0 \tilde{\chi}_j^0, \tag{2.8}$$

24

$$q\bar{q} \to \tilde{l}_i^+ \tilde{l}_j^-, \ q\bar{q} \to \tilde{\nu}_l \tilde{\nu}_l^*, \tag{2.9}$$

$$u\bar{d} \to \tilde{\chi}_i^+ \tilde{\chi}_j^0, \ u\bar{d} \to \tilde{l}_i^+ \tilde{\nu}_l, \tag{2.10}$$

$$d\bar{u} \to \tilde{\chi}_i^- \tilde{\chi}_j^-, \ q\bar{q} \to \tilde{l}_i^- \tilde{\nu}_l^*, \tag{2.11}$$

and QCD reactions:

$$gg \to \tilde{g}\tilde{g}, \ \tilde{q}_i \tilde{q}_j^*, \tag{2.12}$$

$$gq \to \tilde{g}\tilde{q}_i, \tag{2.13}$$

$$q\bar{q} \to \tilde{g}\tilde{g}, \ \tilde{q}_i \tilde{q}_j^*, \tag{2.14}$$

$$q\bar{q} \to \tilde{q}_i \tilde{q}_j \tag{2.15}$$

At the LHC the production through QCD processes should be dominating, unless squarks and gluinos are heavier then 1 TeV. The estimated production cross sections of the main production processes at LHC are shown in Table 2.3.

Table 2.3. Production cross section of supersymmetric particles at LHC for $\sqrt{s} = 14$ TeV.

Process	cross section, fb^{-1}	Process	cross section, fb^{-1}
$pp \to \tilde{g}\tilde{g}$	554	$pp \to \tilde{q}\tilde{q}$	2329
$pp \to \tilde{g}\tilde{q}$	3377	$pp \to \tilde{\chi}_1^\pm \tilde{\chi}_2^0$	258
$pp \to \tilde{\chi}_1^\pm \tilde{\chi}_1^\mp$	140	$pp \to \tilde{\chi}_1^\pm \tilde{q}$	154

The classical $\not{E}_T$ signal for hadron colliders is events with jets and $\not{E}_T$ but no energetic isolated leptons. The lepton requirement allows to reduce background from

SM processes with leptonic W-decays. This signal is a favorite possibility for the first evidence of supersymmetry to be found at LHC.

Figure 2.4. An example of the SUSY decay chain.

The trilepton signal is another possible discovery mode. The signal event consists of three leptons and $\not{E}_T$, and possibly hadronic jets. At LHC such signal can be obtained when one of the squarks or gluinos decay through $\tilde{\chi}_i^{\pm}$ and the other through χ_j^0.

Another possibility is the same-charge dilepton signal. It can occur when gluinos have a large branching fraction to decay into hadrons plus chargino. The produced chargino decays into a final state with a charged lepton, a neutrino and LSP. The probability to have positive and negative charge for the final state lepton are equal, so gluino-gluino and squark-gluino events will often give same charge lepton pairs. The

largest sources of isolated leptons pair in SM produce opposite charge leptons, for example $t\bar{t}$ or W^+W^- production, so the background should be very low. My thesis is aimed at search for a three lepton (e, μ) signature of SUSY event. The signal must contain a lepton pair of the same flavor and different charges plus another lepton. Also, like any SUSY process, it must have large missing energy because of the LSP and at least two high p_T jets. An example of the decay chain is shown in Figure 2.4.

The possible background processes that can produce three leptons are $t\bar{t}$, WZ, Zbb. All these processes can produce three leptons if bosons decay leptonically and b-jets decay semileptonically. Also $Z + jets$ process need to be included, if one of the jets produces a fake lepton. The cross-sections for the signal and backgrounds are given in Table 2.4.

Table 2.4. Cross sections and event yields in 1 fb^{-1} for signal and backgrounds

process	cross section	branching ratio for 3l	N_{events}
SUSY	7.3 pb	0.016	125.8
$t\bar{t}$	833 pb	0.021	17625
Zbb	1492 pb	0.010	37150
WZ	26 pb	0.035	910
$Z + jets$	300 pb	depends on the fake rate	99000

2.6. SUSY Cosmological Constraints.

If R-parity is conserved in SUSY model, and the LSP is neutral, then the LSP is a possible dark matter candidate [12]. Charged LSP would interact electromagnetically and be visible. Thus, possible candidates are the gravitino, the sneutrino, the gluino and the lightest neutralino.

Let us consider the density of certain particles in the universe. At early universe, all particles at thermal equilibrium. Particles are constantly created through different interactions and annihilate against anti-particles with a cross-section σ. These two processes maintain the equilibrium. The particle density changes with time as

$$\frac{dn}{dt} = -3Hn - <\sigma v> (n^2 - n_{eq}^2,) \tag{2.16}$$

The first term represents the dilution caused by the universe expansion, H is the Hubble constant. The second term represents the effect of annihilation, v is a particle velocity and n_{eq} is a density at thermal equilibrium given by a Boltzman distribution. When σ is small particles can not remain in the equilibrium. For most particles there is a temperature T_F when interaction rate become too low. The density at T_F is given by $n_{eq}(T_F)$ and defined by the Hubble expansion. The surviving density depend on σ. The larger the σ is, the larger is a survival number for these kind of particles and the larger contribution they provide to Ω_m.

For large masses of SUSY particles, cosmologically correct models require enhanced annihilation rates, for example because of the accidental mass degeneracies. Also, $\tilde{\chi}_1^0$ annihilation through resonances may take place at large velocities requiring relativistic particles. Within the MSSM models the LSP is almost always the lightest neutralino. Cosmologically interesting LSP relic densities occur only at certain regions in parameter space $m_0 - m_{1/2}$. The possible parameter space is shown at Figure 2.5. The region with small m_0, $m_{1/2}$ is called bulk region. There is no annihilation enhancement here and LSP has mass less than 200 GeV. The region extending from the bulk region to the high $m_{1/2}$ and going on the edge were LSP became slepton is known as "coannihilation tail". In coannihilation region masses of LSP and lightest slepton are almost degenerate and annihilation cross-section is enhanced.The region
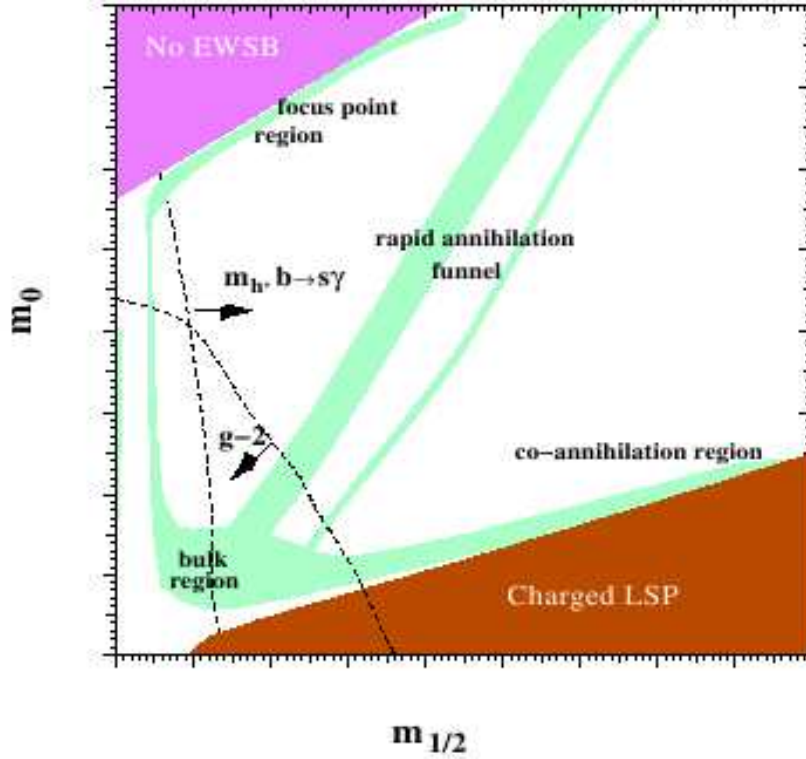
Figure 2.5. Schematic plot of $m_0 - m_{1/2}$ parameter space, [12].

of large m_0, $m_{1/2}$ is known as "rapid annihilation funnel" or "Higgs pole region", because LSP mass is large enough to make annihilation through (s-channel) heavy Higgs boson, increasing σ. Finally, at large m_0 masses, there is a "focus point region" that lies up to the region where there is no electroweak symmetry breaking.

The coannihilation region corresponds to the largest area of the parameter space yielding cosmologically interesting cold dark matter. The masses of the SUSY particles in the region are relatively light and LEP-2 and Tevatron constraints are very severe. As masses of the SUSY particles increase, acceptable density is obtained by

annihilation rate increase. This is possible through the $\tilde{\chi}_1^0 \tilde{\tau} \rightarrow \tau \gamma$ co-annihilation process that becomes enhanced due to near degeneracy between masses of $\tilde{\chi}_1^0$ and $\tilde{\tau}$.

Chapter 3

DETECTOR

3.1. Large Hadron Collider
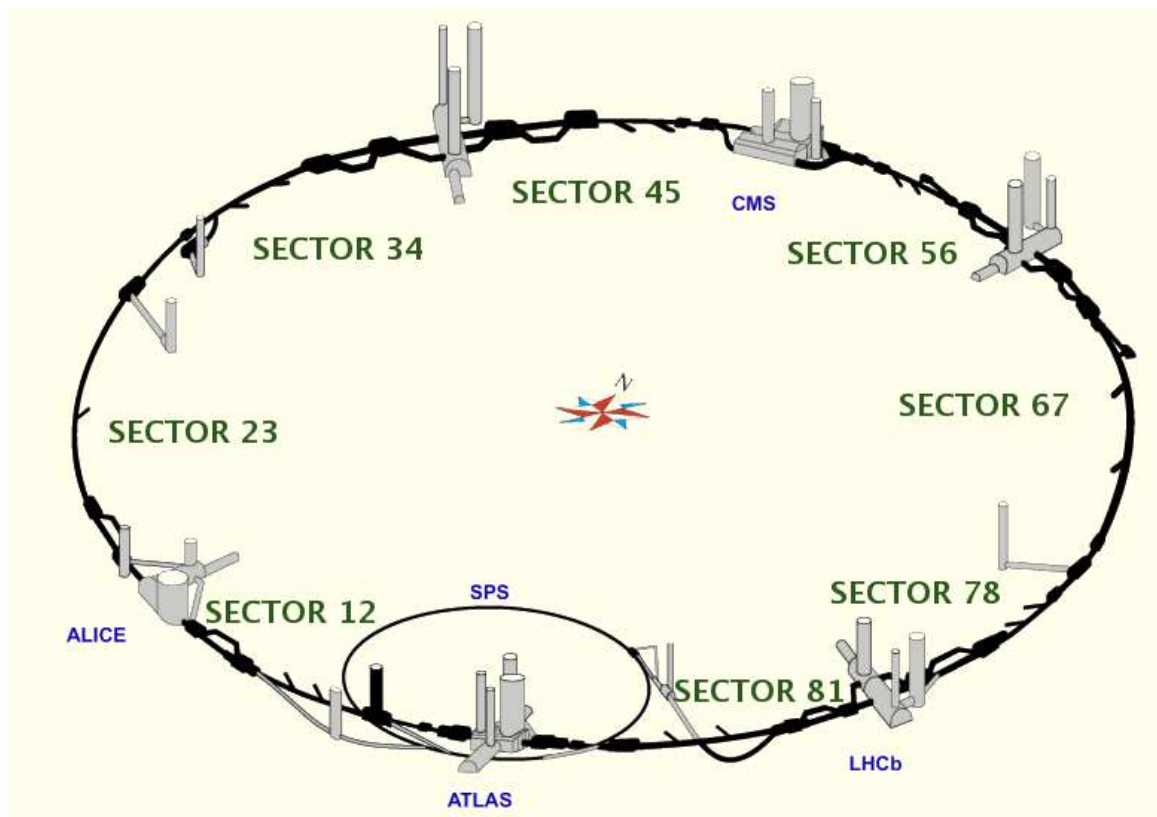
Figure 3.1. The main ring and position of the detectors for the Large Hadron Collider.

The search for new particles often requires larger energy. For, example, the substantial mass of the Higgs boson requires 100-200 GeV of center of mass energy. The

search of new physics is even more demanding. For example, any SUSY signature contains at least two LSP's and requires energy of more than 200 GeV. Because of the high energy losses from synchrotron radiation, e^+e^- colliders are not appropriate accelerators for these tasks.

The solution is to use hadron colliders. The mass of a proton is 2000 times larger then an electron's mass, so synchrotron losses are much lower. Unfortunately, the proton is not a fundamental particle. In the case of an electron collider, two electrons produce a signature through inelastic scattering. All energy of these two electrons goes in the signature. In the case of protons, the interacting particles are not protons, but quarks or gluons with a varying fraction, X_F, of proton momentum. As a result the momentum in the beam direction of these interacting quarks or gluons is unknown and does not balance on a case-by-case basis. Both protons, and their constituent partons, have almost zero momentum in the plane perpendicular to the beam axis, thus total momentum for an event in this plane is zero. That is why at hadron colliders transverse momentum and energy are used.

Another important parameter of the accelerator is its luminosity L. It characterize how many collisions happen during the experiment. $L*\sigma = N_{events}$, where σ is a cross section of the specific process, N_{events} is an average number of events. The higher the luminosity, the more rare and interesting processes can be detected at fixed energy

The new Large Hadron Collider (LHC), built at CERN, will provide both high energy and high luminosity [20]. LHC will have two proton beams of 7 TeV each, providing 14 TeV collision energy - an order of magnitude increase compared to the previously most energetic hadron collider, the Fermilab Tevatron. Two bunches of protons collide every 25 ns, each proton bunch contains $1.15 * 10^{15}$ protons and ultimately, the peak luminosity is expected to reach $L = 10^{34} cm^{-1} s^{-1}$. This can be compared with the best so far at the Tevatron $2.9 * 10^{32} cm^{-1} s^{-1}$.

Protons are obtained by removing electrons from hydrogen atoms in the linear accelerator (LINAC2). LINAC2 generates 50 MeV protons that are then accelerated by the Proton Synchrotron Booster (PSB) up to 1.4 GeV. The next step is the Proton Synchrotron (PS) that produces 26 GeV protons that enter the final Super Proton Synchrotron (SPS) used to increase the energy of protons up to 450 GeV. It uses magnetic field to bent protons and keep them on circular path and electric field to accelerate them. Both fields vary while protons are accelerated to keep them in the beam pipe. Quadrupole and sextupole magnets are used to focus the beam. These protons will be finally injected into the LHC and circulate for 20 minutes before reaching a maximum energy of 7 TeV.

The final stage is built in a 27 km long circular tunnel that is located 50 to 175 m underground and has 6 experiments. ATLAS and CMS are two multipurpose detectors that are aimed at searching for a new physics in a wide range of parameters. LHCb is designed specially for B-physics. TOTEM and LHCf are for studying the forward region particles. LHC can also provide two lead ion beams that will be studied with ALICE detector.

3.2. ATLAS detector

ATLAS is one of the LHC general purpose experiments designed to work at high luminosity [21],[22]. The z-axis is along the beam direction, the polar angle θ is the angle from the beam direction, azimuthal angle ϕ is measured around the beam axis. The $x - y$ plane is the plane transverse to the beam direction. The positive x-axis is pointing from the interaction point to the center of the LHC ring. The positive y-axis is pointing upward. Instead of the polar angle θ the pseudorapidity $\eta = -ln \tan \theta/2$ is usually used. It must allow to make a wide search for new physics. This requires that the detector have:
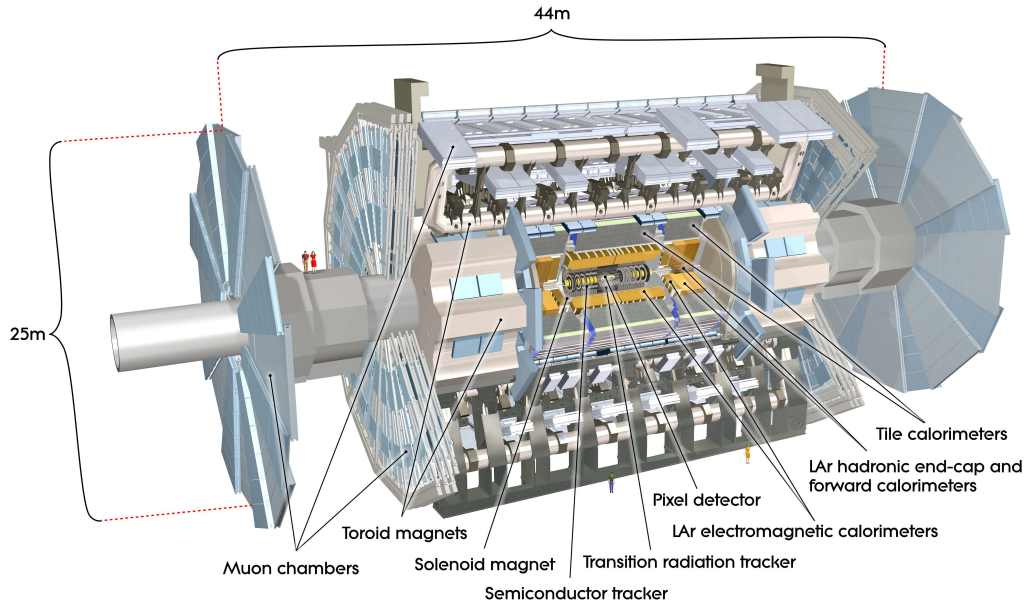
Figure 3.2. A cross section of the ATLAS detector.

- very good and precise calorimeters that allow good energy resolution and position resolution, especially for photons and electrons.

- high-precision muon momentum measurements, being able to determine muon momentum by inner detector only at all luminosities.

- large acceptance in η and ϕ.

- efficient tracking even at high luminosity

- triggering and measuring of particles at low p_T.

3.2.1. Inner Detector.

The Inner Detector measures the momentum of charged particles by measuring the curvature of their trajectory in the magnetic field. The trajectory of the charged

34
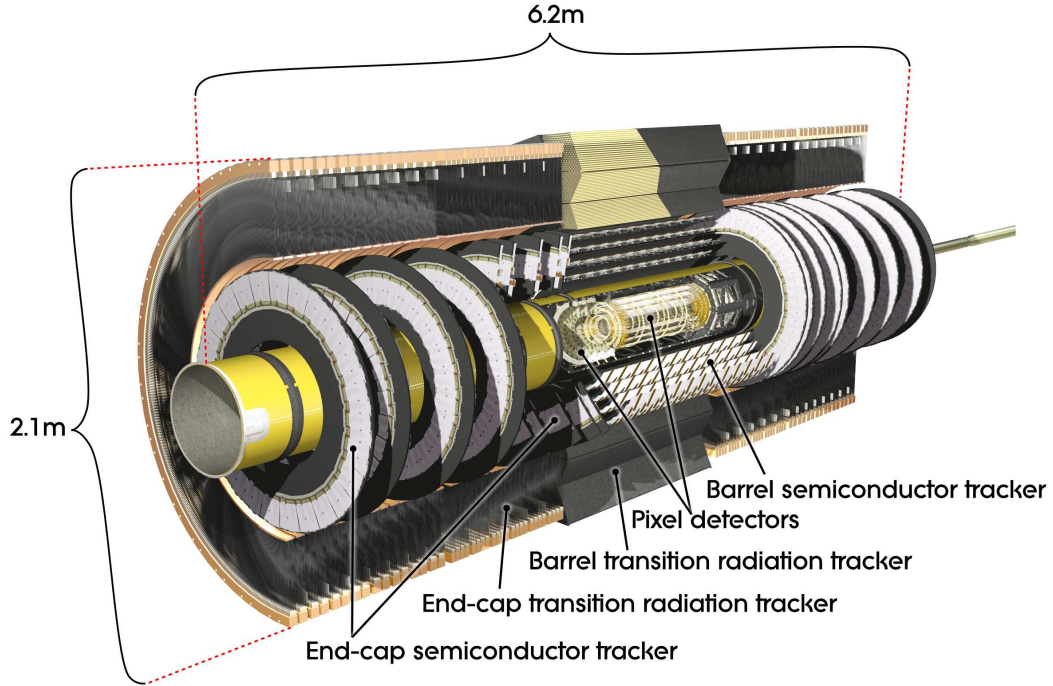
Figure 3.3. Inner Detector.

particle, or its track, is reconstructed using the ionization signal left in several layers of the detector. The ATLAS Inner Detector is made out of three detector types, moving inside out we find: (a) the silicon Pixel Tracker (b) the Semiconductor Tracker (SCT), and (c) the Transition Radiation Tracker (TRT). They cover range $\mid \eta \mid\leq 2.5$.

The pixel detector is designed to provide measurements as close as possible to the interaction point. These measurements must have a very high granularity and precision. The detector consists of three layers of barrel with radii 4 cm, 10 cm and 13 cm and three wheels on each side with radii 11-20 cm. In the detector the semiconductor pixel design is used, placing n^{+}-type readout pixels on the n-type plates. Each pixel has a size 50 μm in $R - \phi$ and 300 μm long. The design has high radiation tolerance.

The SCT consists of four double layers of silicon microstrip detectors in the barrel and nine end cap wheels. In the barrel strips are 12.8 cm long and 80 μm wide. End caps are very similar, but have strips of 12 cm at outer wheels or 6-7 cm at inner wheels. The detector provides measurements in the intermediate region between pixels and TRT and contributes to momentum and vertex measurements. Pixels and SCT together provide precision tracker measurement. SCT provides spatial resolution of 16 μm in $R\phi$ and 580 μm in z. Tracks can be distinguished if they are separated by more than 200 μm.

The TRT is based on straw tube technology. The relativistic particles produce transition radiation when they enter the straws. Transition photons ionize the gas mixture in the tube and this ionization charge is collected on the cathode producing the signal. The TRT contains up to 73 layers of straws. Typically, 7 to 10 hits are expected from electrons above 2 GeV. Each straw is 4 mm in diameter and up to 144 cm in length. It contains a non-flammable gas mixture of 70% Xe, 20% CO_2 and 10% CF_4. The detector has a spatial resolution of 170 μm per straw.

3.2.2. ATLAS Magnet System.

The ATLAS superconducting magnetic system consists of a central solenoid (CS) providing the Inner Detector with a magnetic field. This is surrounded by three large barrel toroids (BT) generating magnetic fields for the muon spectrometer and two end-cap toroids (ECT) that are inserted in the barrel toroids at each end. The magnetic system has total length 26 m and diameter 22 m.

The central solenoid is designed to provide a 2 T axial field. The toroids provide a non-uniform magnetic field that has average value 0.5 T in the barrel region and varies from 0.2 to 3.5 T in the end-cap region. The field performance in terms of bending power is characterized by $\int Bdl$, where B is the azimuthal field component

and integral is taken on a straight line trajectory between the inner and outer radius of the toroids. The BT provides 2-6 Tm and ECT gives 4-8 Tm in the $0 \leq \mid \eta \mid \leq 1.3$ and $1.6 \leq \mid \eta \mid \leq 2.7$. In the region $1.3 \leq \mid \eta \mid \leq 1.6$ where two magnets overlap the bending power is lower.

3.2.3. Calorimeters.
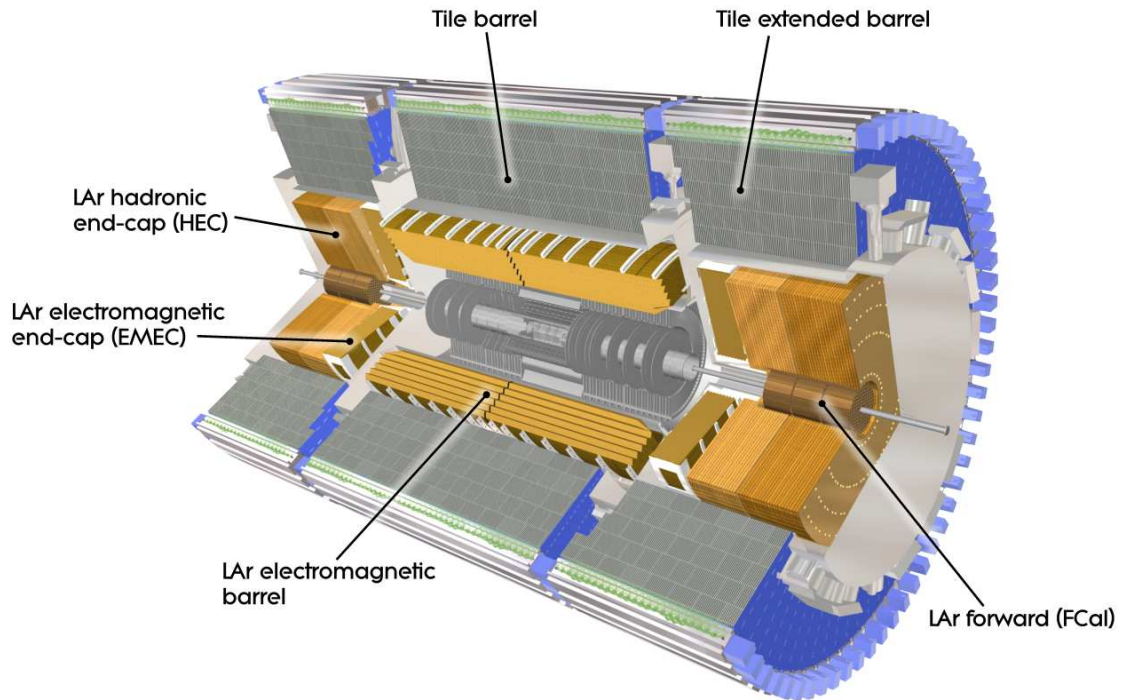
Figure 3.4. ATLAS Calorimeters.

Calorimeters perform energy measurement of an incident particle by total absorption and a conversion of the particle's energy into a measurable signal. The calorimeter design can be optimized either towards the detection of electromagnetic or hadronic showers. The electromagnetic calorimeters are optimized for detection

of electrons and photons while the hadronic calorimeters are optimized to measure showers produced by strongly interacting particles.

Calorimeters are also grouped into homogeneous and sampling ones by their construction properties. Homogeneous calorimeters consist of only active medium. Active medium is a material where the lost energy is converted into a measurable signal. In sampling calorimeters, layers of active medium alternate with layers of absorber. Absorber re-absorbs most of freed charge, but only a fraction (the "sampling fraction") makes it into the active medium. By knowing properties of the absorber material and the signal from active layers the total energy can be reconstructed.

3.2.3.1. Electromagnetic calorimeter.

At energies above 1 GeV, an electron loses most of its energy through bremsstrahlung. The bremsstrahlung photon passing through the matter of the calorimeter and undergoes conversion into an electron-positron pair. Each electron and positron, in turn, can again emit bremsstrahlung photons. These two processes repeat multiple times and produce a cascade of electrons and photons with decreasing energy. This cascade is called an electromagnetic shower. Radiation length X_0 is the mean distance over which a high-energy electron reduces its energy by a factor of e by bremsstrahlung, and 7/9 of the mean free path for pair production by a high-energy photon. X_0 is very useful to describe the size of the shower.

The ATLAS electromagnetic (EM) calorimeter is designed to trigger on and to provide precision measurements of the energy of electrons, photons and missing E_T [25]. Beside the usual calorimeter tasks of energy measurements, it also provides angular measurements and participates in the particle identification.

The ATLAS EM calorimeter consists of a barrel part that covers pseudorapidity range $|\eta| < 1.475$ and two end-caps that cover a range $1.375 < |\eta| < 3.2$. The barrel

and the end-caps cover a full 2π range in the azimuthal angle ϕ. The total thickness of the EM calorimeter is above 24 X_0 for the barrel and above 26 X_0 for the end-caps and is divided into four layers in depth. This division allows to study longitudinal profile of the shower that is needed for particle identification.
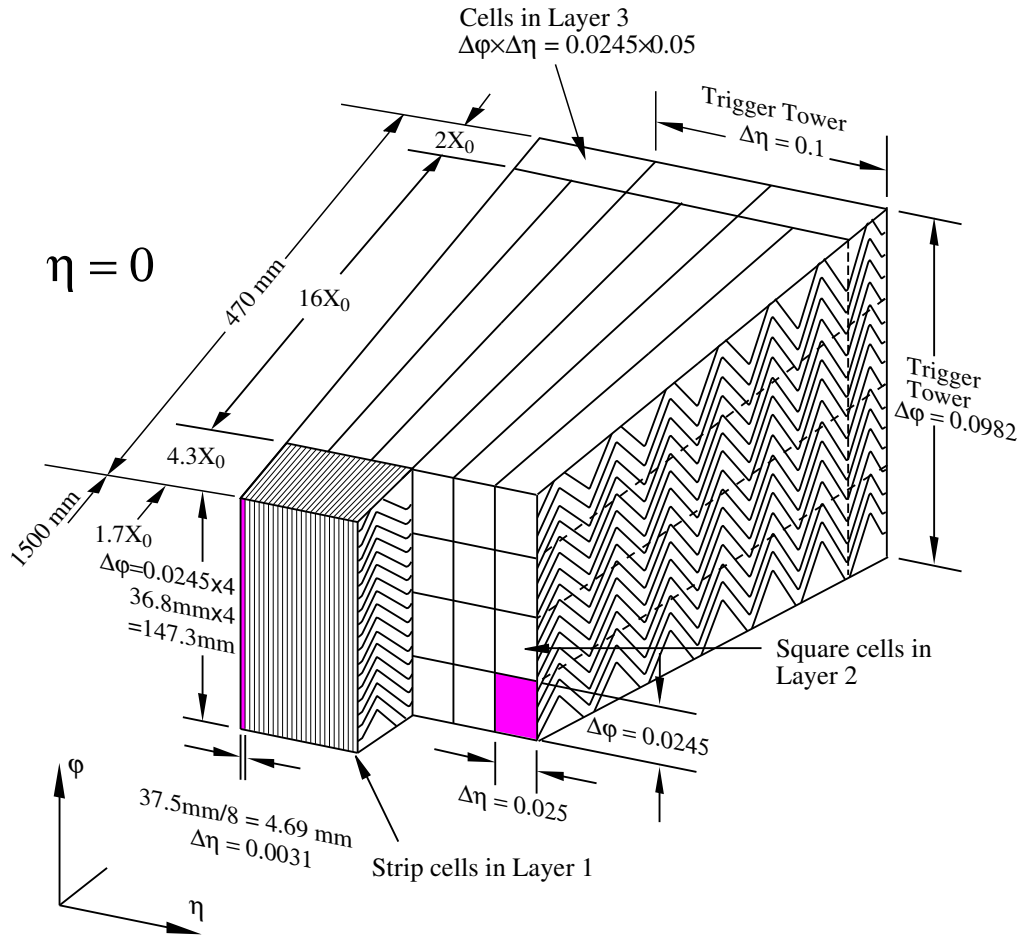
Figure 3.5. "Accordion-shaped" calorimeter cell. You can also see four layers in depth with different size of cells.

"Accordion-shaped" electrodes are used for all electromagnetic calorimetry. It covers the pseudorapidity interval $|\eta| < 3.2$. A picture of the cell is shown in Fig. 3.5. The "accordion-shaped" electrodes collect a signal that is independent of the incident

angle of the particle. In the ATLAS calorimeter Liquid Argon is used as an active medium and lead/stainless-steel plates are used as an absorber. The absorber plates have the thickness varying from 1.1 mm to 2.2 mm depending on the region. They are separated by the 2 mm gaps filled with liquid Argon. The shower of a charged particle passing through the liquid Argon produces an ionization. The total charge collected on the cathodes is proportional to the energy deposited in the calorimeter.

3.2.3.2. *Hadron calorimeter.*
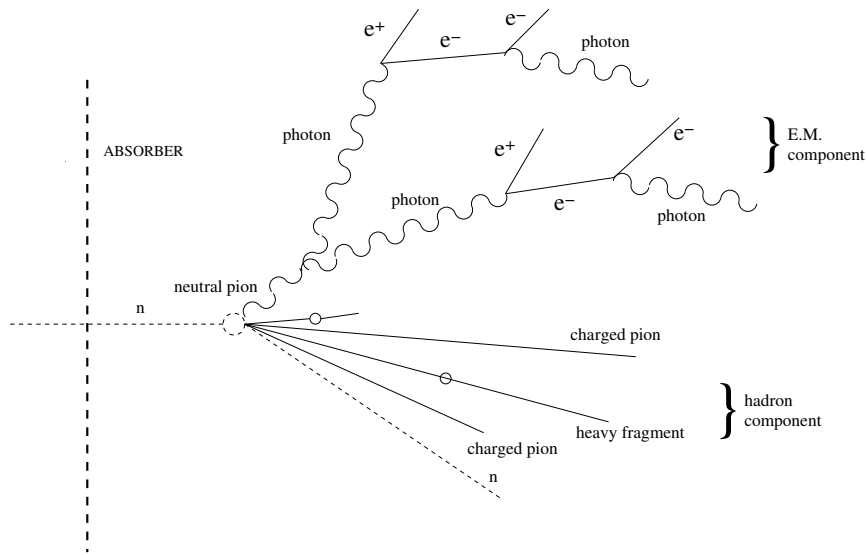
Figure 3.6. Hadronic shower development.

Hadronic showers are much more complicated than the electromagnetic ones. They result from the sequential inelastic hadronic interactions that produce cascades of different particles. A schematic illustration of a hadronic shower is shown in Fig. 3.6. Because the nuclear cross-sections are much smaller than for photon conversion, the hadronic showers start later in the material than the electromagnetic showers and,

therefore, the hadron calorimeter must be more massive than the electromagnetic calorimeter. A part of the hadronic shower energy is released through an electromagnetic component coming mostly from prompt $\pi^0/\eta \to \gamma\gamma$ decays. A longitudinal shower development is described by the interaction length λ, which is a mean free path between two inelastic nuclear interactions.

The ATLAS hadronic calorimeter covers a large η range $|\eta| < 4.9$ and consists of three different parts: Tile calorimeter, LAr hadronic end-cap calorimeter (HEC) and forward calorimeter (FCal)[22] .

The Tile calorimeter covers the range $|\eta| < 1.7$ and has total length 11.6 m, inner radius 2.28 m and outer radius 4.25 m. This is a sampling calorimeter using steel as an absorber and scintillator as an active material. The optical signal from the scintillator is read by wavelength shifting fibers into two separate photomultipliers. The depth of the Tile calorimeter is 7.4λ.

LAr calorimeters were chosen for the hadronic end-cap (HEC) calorimeter (1.5 < $|\eta| < 3.2$) and high-density forward calorimeter (FCal) (3.1 < $|\eta| < 4.9$). The HEC consists of two wheels with outer radius 2.03 m. Each FCal consists of one electromagnetic module (FCal1) and two hadronic modules (FCal2 and FCal3). Total depth of the FCal calorimeters is 9.94λ.

3.2.3.3. LAr Read out electronics.

A passage of a high energy particle generates a current signal in the calorimeter cell. This signal is called a physics signal. It is triangular in shape as a function of time. The integral of the signal over time or the total charge of this signal is proportional to the energy deposition. The LHC will have a bunch crossing every 25 ns, but LAr calorimeters have an electron drift time 400 ns for electromagnetic calorimeter and 60 ns for FCal (because the gap size is smaller in FCal). The drift
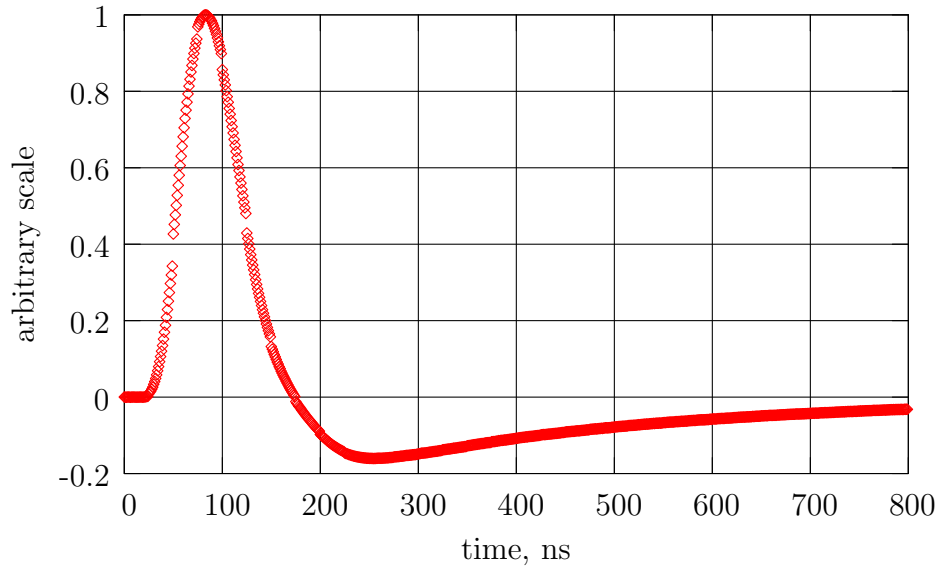
Figure 3.7. Master waveform.

time is too long and leads to overlap of several signals, so it should be somehow reduced. The solution is to use not the signal, but its derivative. The shape of the derivative is shown at Figure 3.7. The peak value of the differentiated signal is proportional to its total charge, i.e., to the energy deposited in the cell, see [28].

The calorimeter is placed in a cryostat that maintains a controlled low temperature necessary for the liquid Argon. The signal collected on the electrodes is transmitted through a special cable system called a feedthrough outside the cold zone and then to the Front End Board (FEB). On the FEB, the current signal is first converted to voltage and amplified. Then the signal is differentiated by a shaping amplifier (shaper). In ATLAS, the shaper output signal is sampled every 25 ns and stored in a special analog pipeline, where it waits for the decision of the trigger. If the event is triggered, a 12 bit ADC digitizes five samples of the signal in such a way that
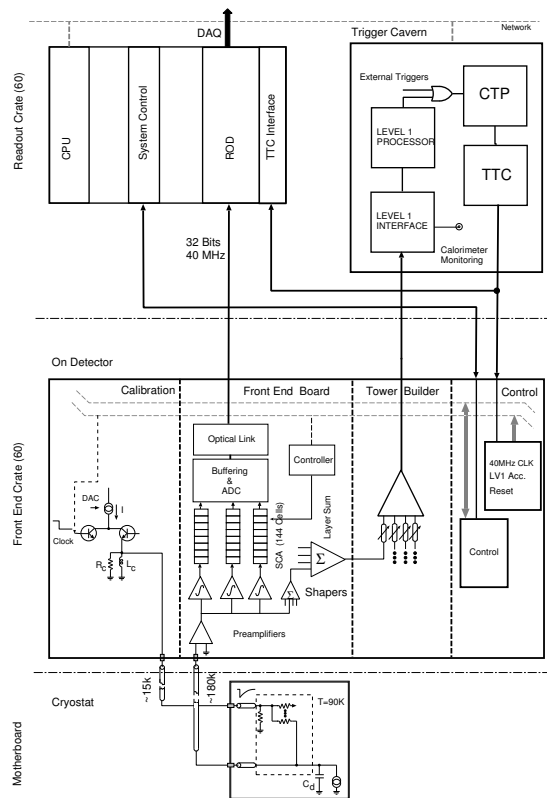
Figure 3.8. Diagram of the LAr read out electronics chain.

the third sample is within several nanoseconds from the peak. The shaping amplifier provides output with three different gains (1 - low, 10 - medium, 100 - high). These three gains allow us to use ADC more effectively by reducing the rounding error for small signals. The electronics automatically choose an appropriate gain value for the ADC input. The digitized signal samples are sent to the Read Out Driver (ROD) board. The signal after the ADC we call a waveform. An example of the waveform is shown on plot 3.7.

3.2.3.4. *Optimal Filtering.*

In an ideal case, knowing just the peak value of the signal should be enough to calculate the corresponding energy. But in practice we have to take into account the noise and the time jitter. Optimal filtering minimizes the effect of the noise and that of the jitter by using five points or samples of the signal [28].

If we assume that we know the signal shape and that the only uncertainties are the overall amplitude, A, and the time of origin, τ, then the signal samples are given by

$$S_i = Ag(t_i - \tau) = Ag_i - A\tau g_i' + n_i,$$

where g is the corresponding master waveform, g_i and g_i' are values of the master waveform and its derivative at time $(t_i - \tau)$, t_i is the sampling time and n_i is the noise component. Our goal is to find A and τ from the set of samples S_i, minimizing the effects of the noise. To do this, we define the coefficients a_i and b_i that are called optimal filtering coefficients (OFC). Using a_i and b_i, we can form two linear sums u and v:

$$u = \sum a_i S_i; \qquad v = \sum b_i S_i.$$

We choose coefficients in such a way that the expectation value of u is equal A and that of v is equal to $A\tau$. Thus we have

$$A = <u> = \sum(Aa_ig_i - A\tau a_i g_i' + <n_i>)$$
$$A\tau = <v> = \sum(Ab_ig_i - A\tau b_i g_i' + <n_i>)$$

The random noise will average to zero leading to following constraints on a_i and b_i:

$$\sum a_i g_i = 1 \qquad \sum a_i g_i' = 0$$
$$\sum b_i g_i = 0 \qquad \sum b_i g_i' = -1.$$

44

The variances V of the parameters u and v are given by

$$V(u) = \sum a_i a_j < n_i n_j >= \sum a_i a_j R_{ij}$$
$$V(v) = \sum b_i b_j < n_i n_j >= \sum b_i b_j R_{ij}.$$

The expectation value $< n_i n_j >= R_{ij}$ is the noise autocorrelation function evaluated at a time $t_i - t_j$.

In order to obtain A and $A\tau$, we need to minimize the variances of u and v while satisfying the constraints for the optimal filtering coefficients. This can be done by using the method of Lagrange multipliers. The solution for OFC in a matrix form is

$$a = \lambda R^{-1} g + \kappa R^{-1} g'$$
$$b = \mu R^{-1} g + \rho R^{-1} g'$$

Here, λ, κ, μ and ρ are the Lagrange multipliers, $R = R_{ij}$ is the autocorrelation matrix and a, b, g, and g' are column vectors of optimal filtering coefficients, master waveform and its derivative respectively.

The solution for the Lagrange multipliers has the form

$$\lambda = Q_2/(Q_1 Q_2 - Q_3{}^2) \qquad \kappa = -Q_3/(Q_1 Q_2 - Q_3{}^2)$$
$$\mu = -Q_3/(Q_1 Q_2 - Q_3{}^2) \qquad \rho = Q_1/(Q_1 Q_2 - Q_3{}^2),$$

where $Q_1 = g^+ R^{-1} g$, $Q_2 = g'^+ R^{-1} g'$ and $Q_3 = g'^+ R^{-1} g$. When we know the OFC's, the amplitude A and the start time τ can be easily calculated from the signal samples using equations:

$$A = \sum a_i S_i \quad A\tau = \sum b_i S_i.$$

45

3.2.3.5. Front End Crate Test.
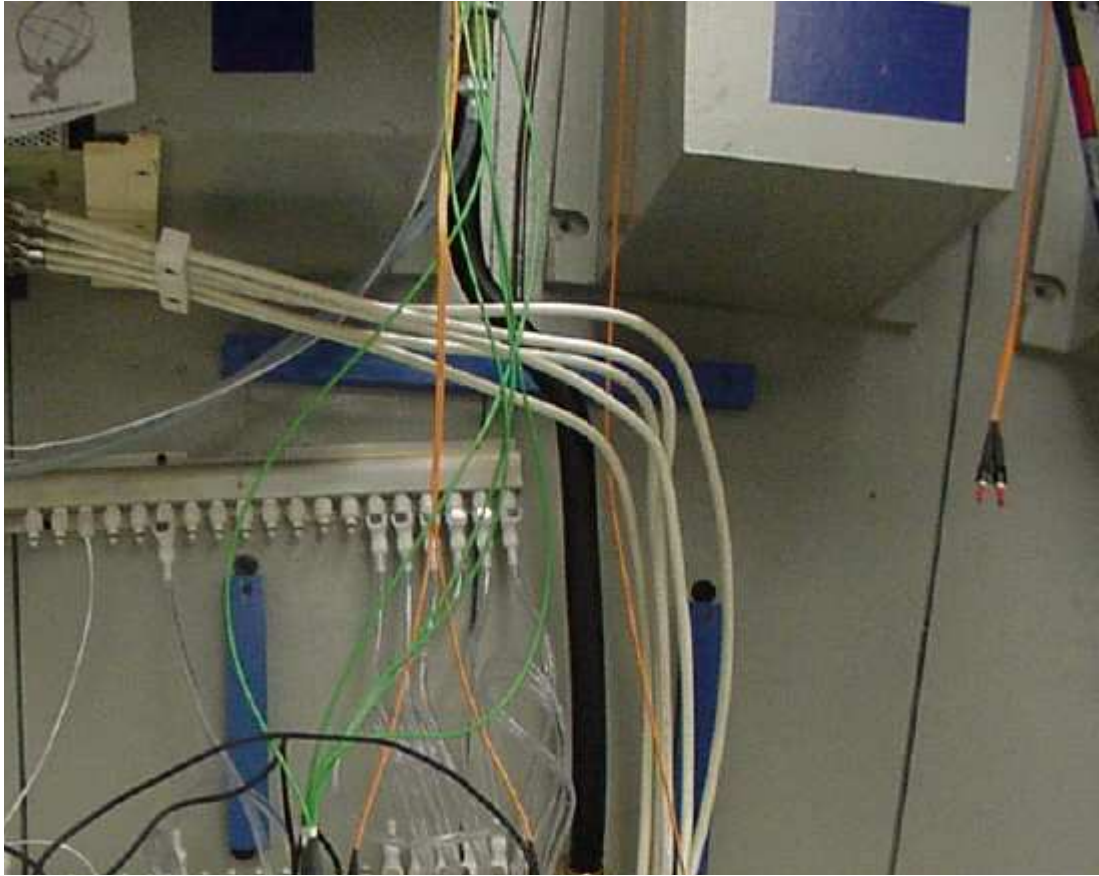
Figure 3.9. Photo of the FECT setup.

The Front End Crate Test (FECT) was carried out to test the complete electronics chain [26] of the ATLAS Liquid Argon calorimeter. FECT description is mostly taken from [27]. A photo of the FECT setup is shown in Fig. 3.9. The setup, located at BNL, consisted of a complete unit of the electronics chain filling half of a front end crate. The effect of the real cells was simulated by appropriately chosen capacitors. The system contained 14 FEB's capable of reading 128 channels each,

and the necessary control and service boards (crate controller, calibration board, tower builder board, clock distribution board, and monitor board). The boards were well shielded from the external noise by a Faraday cage. The FEB's were separated into four groups. Each group processed signals corresponding to the one layer of the calorimeter. There was one board for the presampler (PS), seven boards for the front layer (F0 - F6), four boards for the middle layer (M0 - M3) and two boards for the back layer (B0 - B1). Because real cells were not available during the test, the calibration board was the only source of the input signal. Because calibration signal and physics signal are injected in different points in the readout chain, the shape of the waveform for these signals is different. The results are valid only for the calibration signals and additional corrections are needed to compare them to those for the real data.
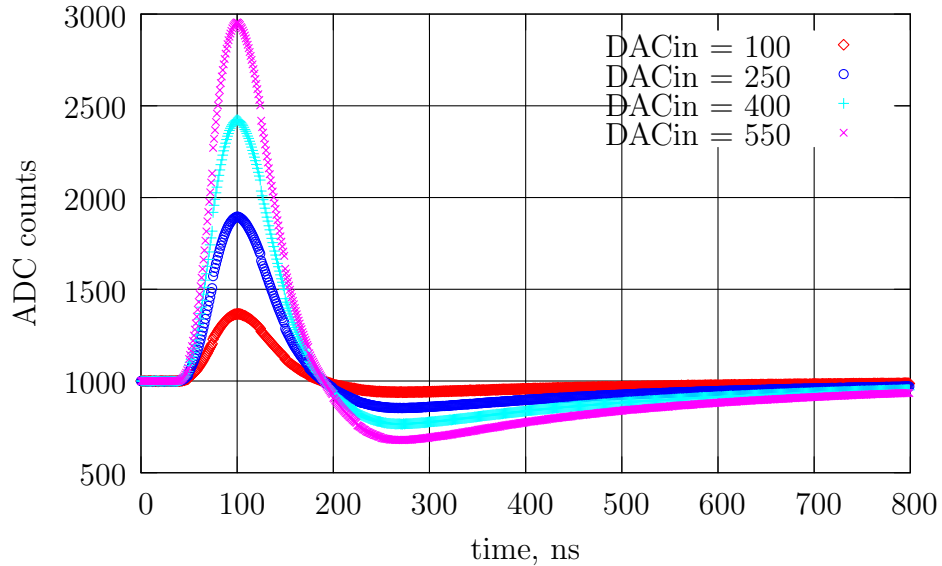
Figure 3.10. The calibration waveforms corresponding to different DACin.

47

In order to reconstruct the energy deposited in the calorimeter from a calorimeter signal, we need to know the Optimal Filtering Coefficients (OFC). To obtain the OFC, we need to know the master waveform, its derivative and the noise autocorrelation function. All this information can be obtained from the calibration procedure.
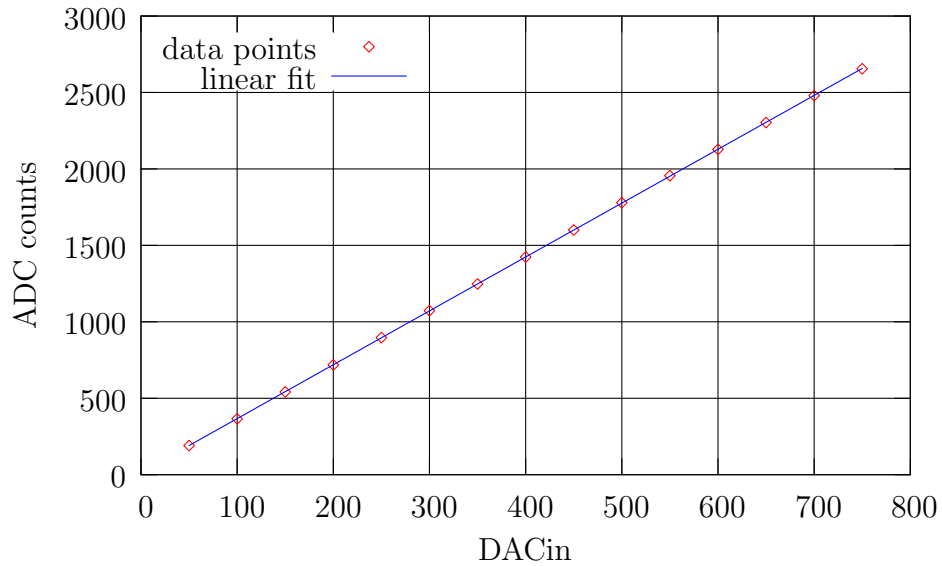
Figure 3.11. An example of the master waveform fit.

The calibration system allows for the precise measurements of the calibration waveform for each channel. The calibration waveform is a waveform that is generated when the input signal originates from the calibration board and not from the physics process. The read-out system allows us to measure the signal every 25 ns. The calibration board provides an identical input signal as many times as we want. By delaying the input signal we can sample a different set of points of the same waveform. This procedure is called a delay run. During FECT we took 200 identical events for each point of the each calibration waveform. The value of the waveform was obtained

by averaging over these identical events to minimize random fluctuations.

To calculate a master waveform we need to measure several calibration waveforms with different values of the amplitude or DACin. Four calibration waveforms corresponding to different DACin are shown in Fig. 3.10. Next, for each point of the master waveform we fit to a linear function the calibration waveform values at this point versus the DACin values corresponding to these calibration waveforms. An example of the fit is shown in Fig. 3.11. The slope of the fit represents a value of the unnormalized master waveform. The waveform is normalized in such a way that its peak value is equal to one. After the normalization we get the master waveform that is used for the OFC calculation. A typical master waveform and its derivative are shown in Figs. 3.7 and 3.12, respectively
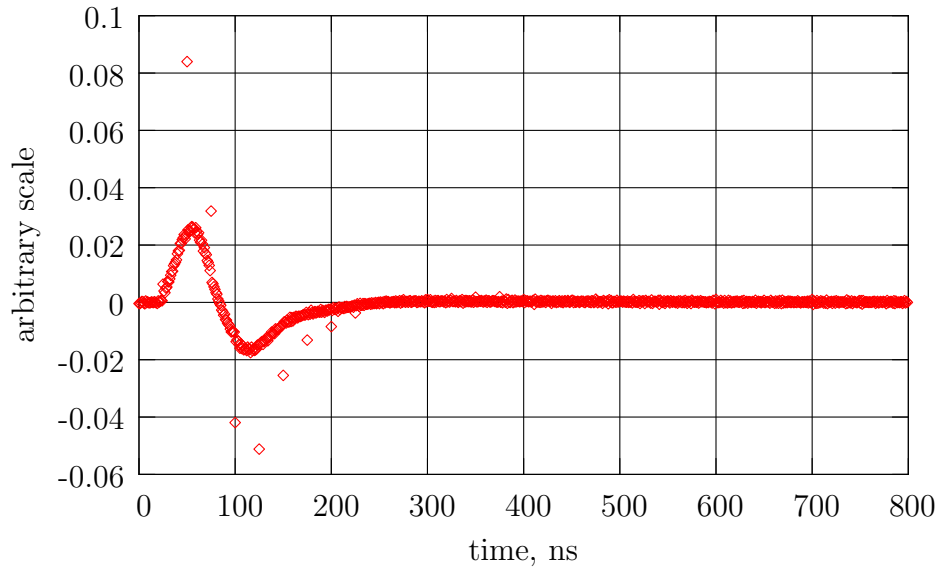
Figure 3.12. Derivative of the master waveform.

In order to calculate the noise autocorrelation matrix, we took data during a special run with the readout system turned on but without any input signal. In this case the only source of the signal was the noise in the electronic chain. We took 100,000 events, and obtained the autocorrelation matrix by averaging over these events. The quantity R_{ij} is equal to the product of response in the same channel at times t_i and t_j. $R_{ij} = < n_i n_j >$. We took separate runs to obtain R_{ij} for all three gain values.
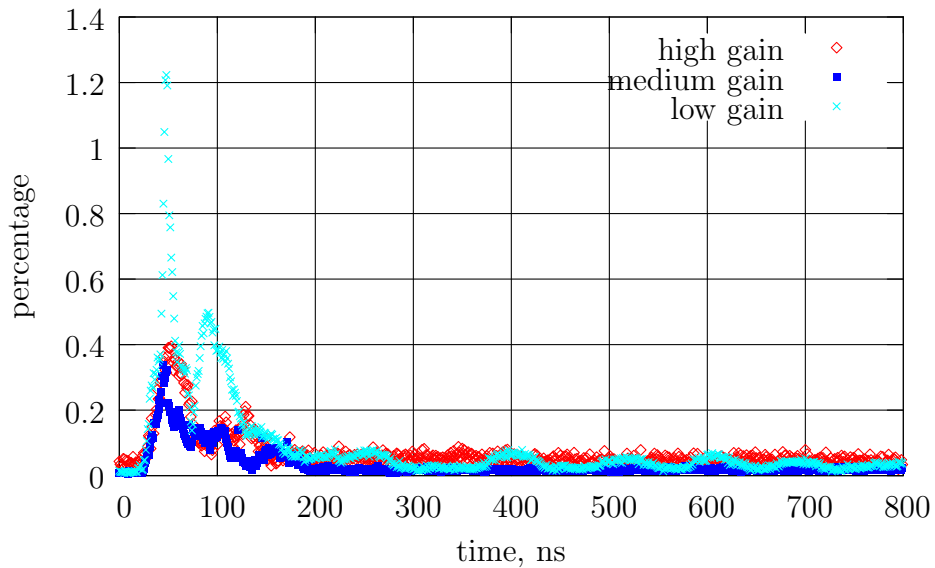
Figure 3.13. Integral nonlinearity of the master waveform fit.

The optimal filtering method uses an assumption that the system is linear. The ATLAS requirement is that the integral nonlinearity of the master waveform fit must be smaller than 1%. The integral nonlinearity is the absolute value of the maximum difference between the fit and the data divided by the maximum of the largest calibration waveform in the channel. In the Fig. 3.13, you can see a typical nonlinearity

50

for the high gain. High and medium gain data satisfy the requirement. Low gain data have some problems with linearity, that will be discussed later.
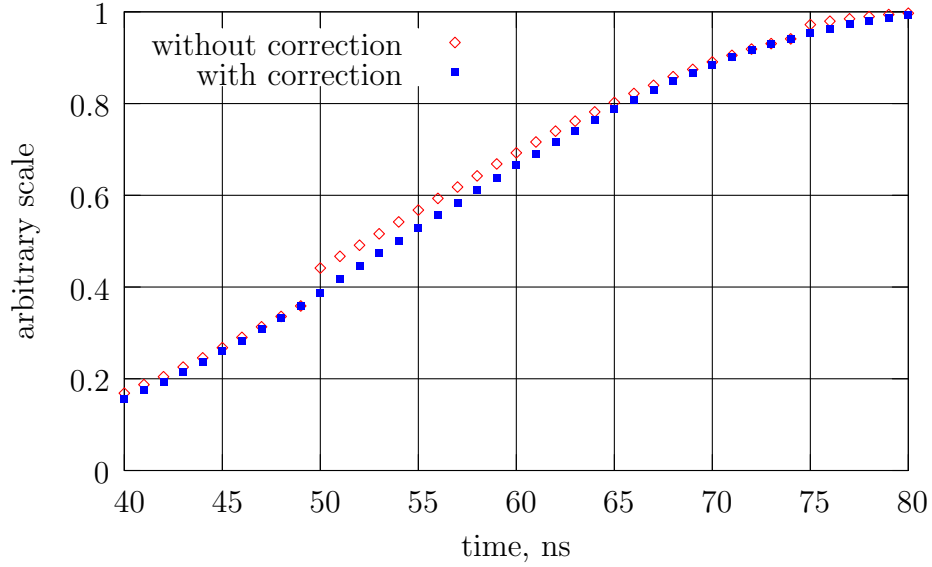
Figure 3.14. Part of the master waveform without correction and with different corrections

The master waveform shown in Fig. 3.7 has discontinuities every 25 ns. We have verified that these gaps are caused by the fact that, during the delay run, the actual delay steps are not exactly equal to 1 ns. The corresponding time error is cumulative and proportional to the delay value. As a consequence, we put the master waveform points in the wrong time positions. Thus the point that corresponds to a delay value of 24 ns is substantially shifted in time while its neighboring point corresponding to a delay 0 is not shifted at all. Hence, the difference in time between these two adjacent points can be much bigger than the nominal value of 1 ns creating the observed discontinuities of the master waveform.
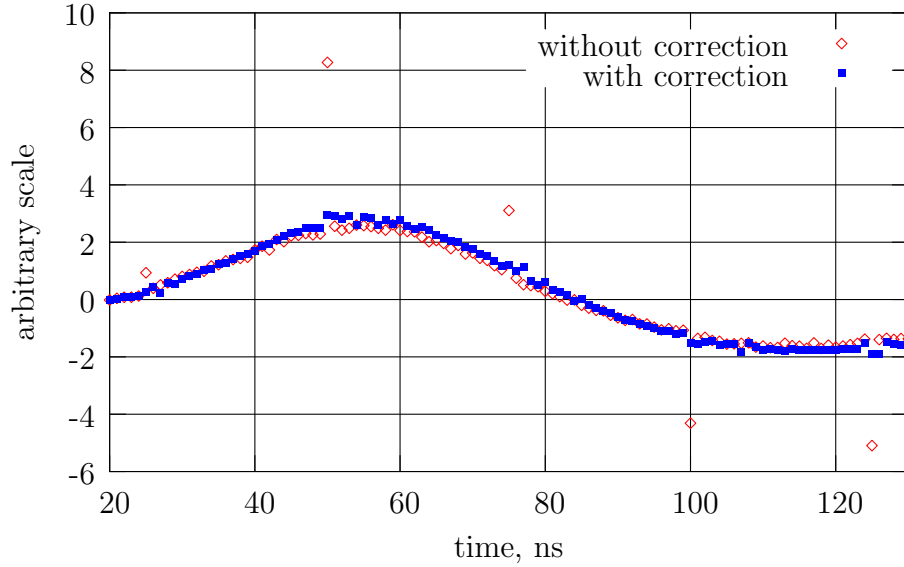
Figure 3.15. Derivative of the master waveform with and without corrections

During the FECT, we made measurements of the exact delay values coming from the calibration board using a scope. We then corrected the corresponding time intervals for our measurement. The corrected master waveforms and their derivatives are shown in Figs. 3.14 and 3.15 together with the original, uncorrected measurement. The corrections compensate well for the discontinuities in the waveform and its derivative. To avoid this problem in the subsequent measurements, it was decided to use delay values from the TTCRx board.

An unexpected dependence of the root-mean-square (rms) for the calibration waveforms on the input DACin values was found for the PS board at high and medium gains and for all boards at low gain. The source of the problem has been identified to be a cross-talk between calibration channels. PS board is more sensitive to the cross-talk, but at low gain when the current in the channels is the largest on the

calibration board, it affects the other layers as well, see [27]

There was no physics signal during FECT and therefore it was impossible to make a measurement of the most important characteristic of the system, i.e. of its energy resolution. We could make, however, a reconstruction of the DACin that plays the same role for the calibration signal as the deposited energy for the physics signal. From the parameters of the system we can calculate the current corresponding to the calibration signal and the energy that must be deposited in the cell to produce this current signal. [25] Thus, we can reconstruct DACin in units of energy (electron-volts). All following results are obtained for this reconstructed "energy".
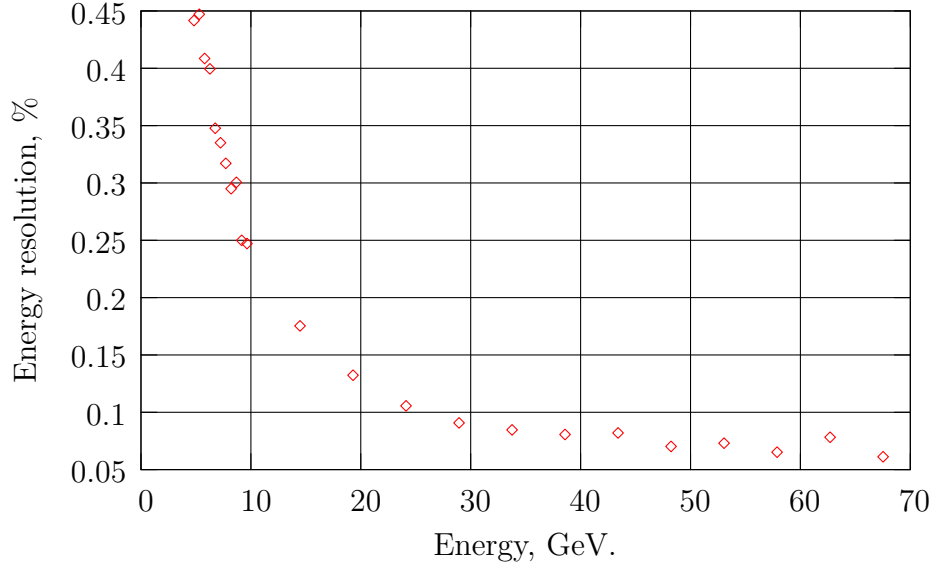
Figure 3.16. Example of energy resolution for medium gain.

The examples of the energy resolution for the calibration signal is shown in Fig. 3.16. Energy resolution is usually parametrized as

$$\sigma/E = a/\sqrt{E} \otimes b/E \otimes c,$$

53

where a is a stochastic term, b is a coefficient of the noise term, and c is a constant term.

In order to reach the new physics discovery potential there are several requirements listed in the Technical design Report [21] that describe the energy resolution, the noise and the constant terms of the calorimetric measurements. Contribution to the constant term from the electronics must be below 0.25% (total constant term must be below 0.7%). The measured values of the constant terms for all three gains are shown in Figs. 3.17-3.19. The requirements on the noise term are less strict and the limit is below 200-400 MeV for different space positions. The noise term results are shown in Figs. 3.20-3.22. The stochastic term is defined by properties of the calorimeter itself and could not be investigated in the FECT because no real calorimeter cells were there.
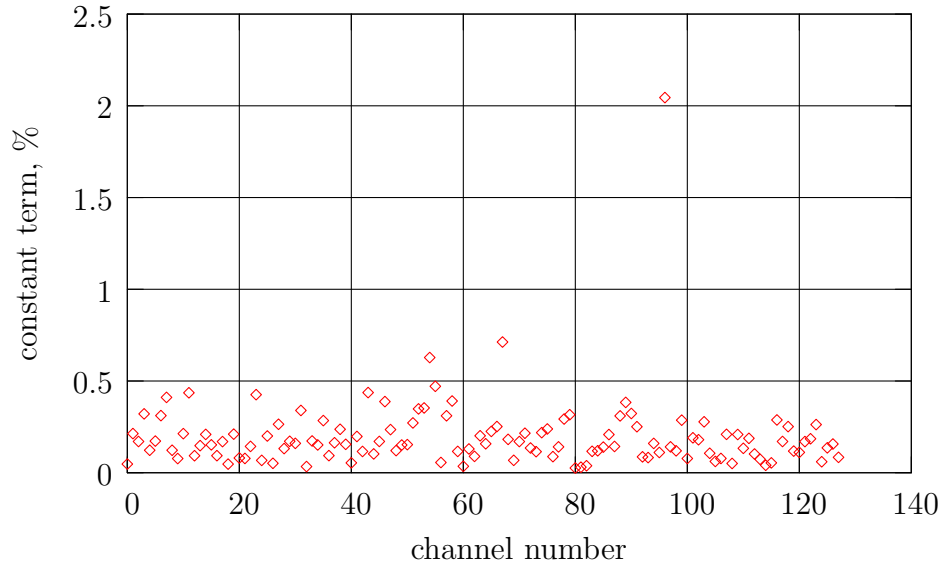
Figure 3.17. Constant term for high gain.
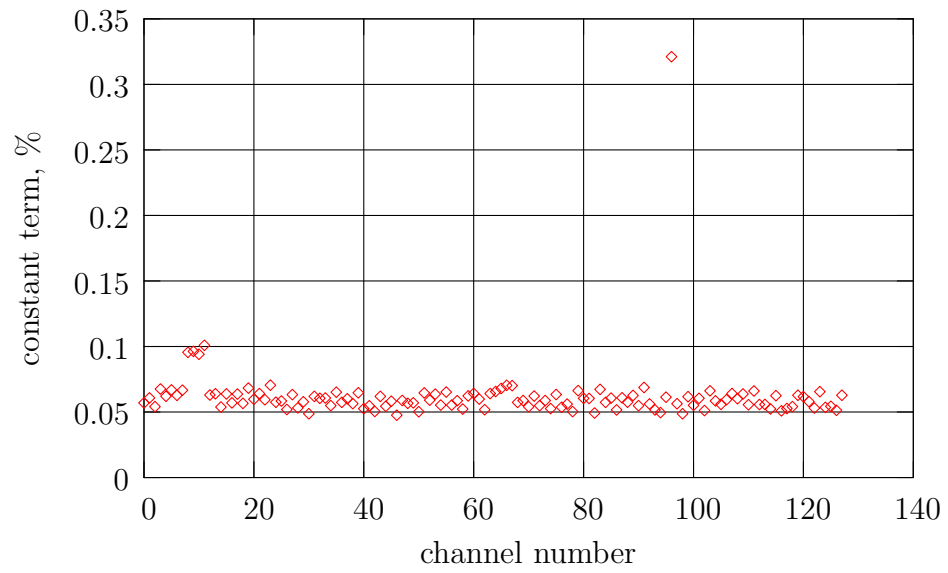
Figure 3.18. Constant term for medium gain.
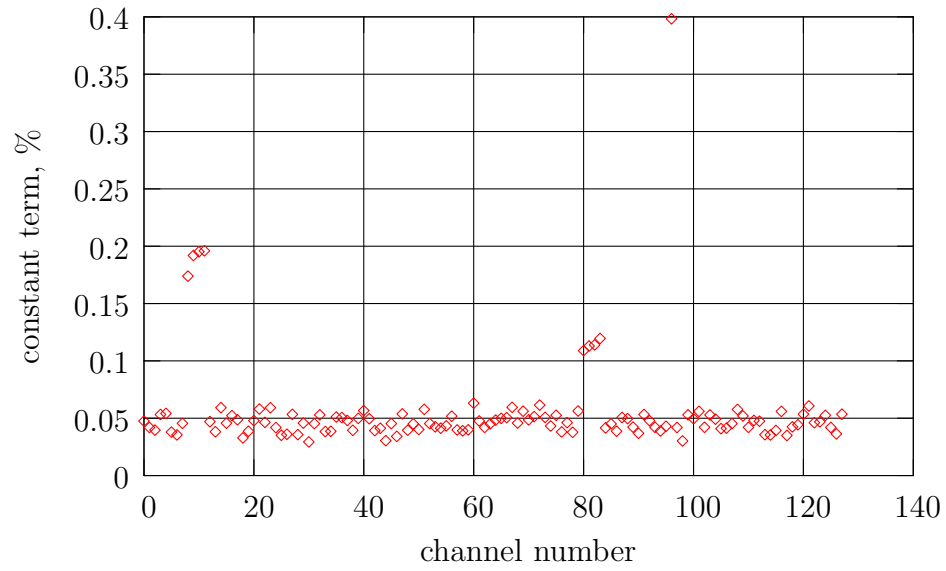
Figure 3.19. Constant term for low gain.

The requirements are made for energy resolution of a particle. A particle deposits its energy in several calorimeter cells or a cluster. All calibration results here are made for the one cell, so a correction will be needed for real detector performance. Pileup is also not included.
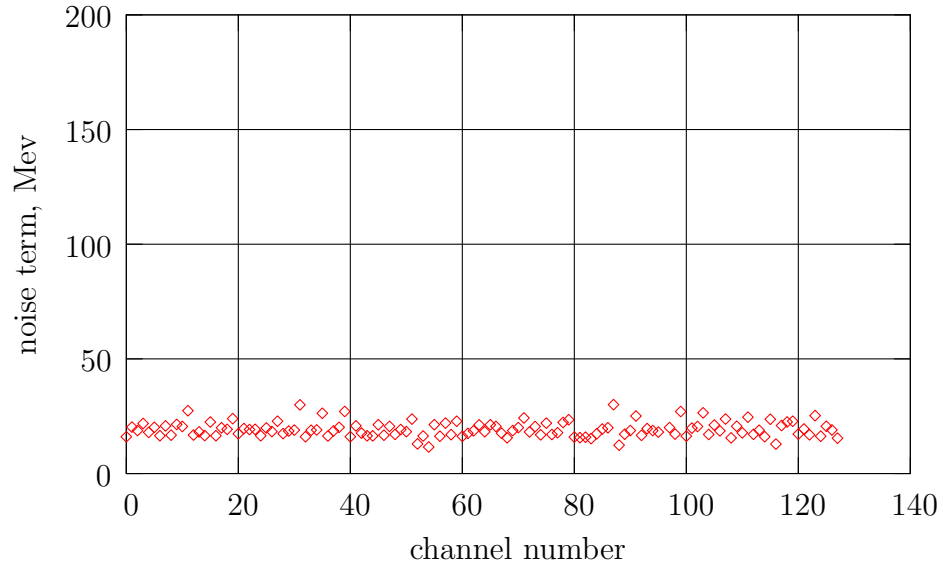
Figure 3.20. Noise term for high gain.

The medium gain data satisfy and exceed all requirements. The constant term for the high gain data was measured to be up to 0.5%; the TDR requirement is 0.25%. However, this result is from small signals.

The low gain data have some problems with the noise term, but they come from cross-talk between the calibration channels. The low gain data still satisfy the constant term requirements even with large cross-talk.

3.2.4. Muon spectrometer.

The ATLAS muon spectrometer is designed for muon detection [22]. Ionization signal left in muon chambers allows to reconstruct a muon track and find its momentum using the deflection in the magnetic field. Muon reconstruction process also use muon track information from the Inner Detector.
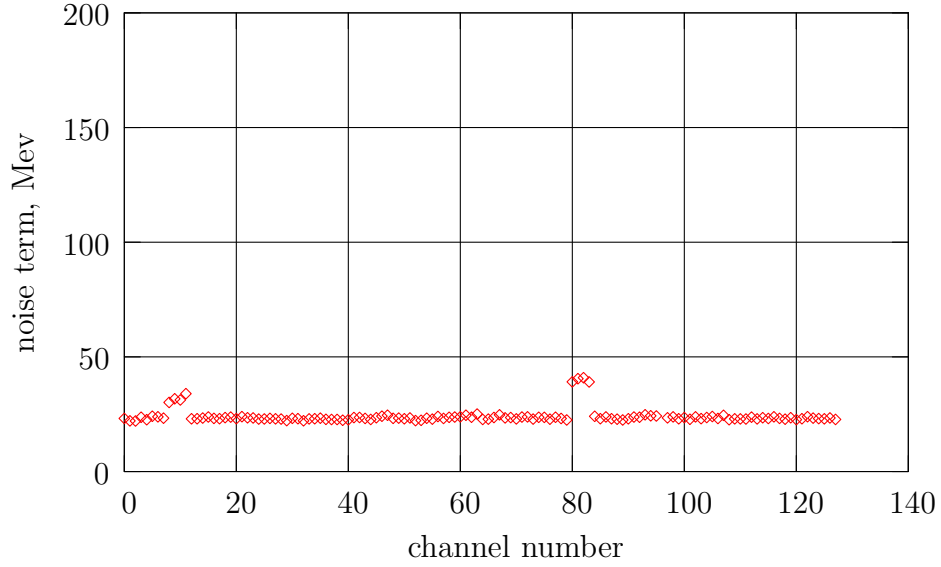
Figure 3.21. Noise term for medium gain.

The muon chambers have three layers in the barrel region (called 'stations') and stations in end-cap wheels. Over most of the η range, track measurements are provided by Monitored Drift Tubes (MDT). Cathode Strip Chambers (CSC) with higher granularity are used in the regions where the higher precision is needed (at large η and closer to the interaction point).

The muon spectrometer is designed to provide a full η coverage. All particles are required to give hits in three muon stations. In the barrel, particles are measured at the inner and outer boundaries of the magnetic field and inside the field volume, to provide the best spatial resolution. The end-caps do not allow to place a station inside the field volume, so muon chamber end-caps are designed to get the best possible resolution from a point-angle measurement. Three layers of barrel at radii 5, 7.5 and 10 m provide coverage for $|\eta| < 1.0$. The end-cap chambers cover the
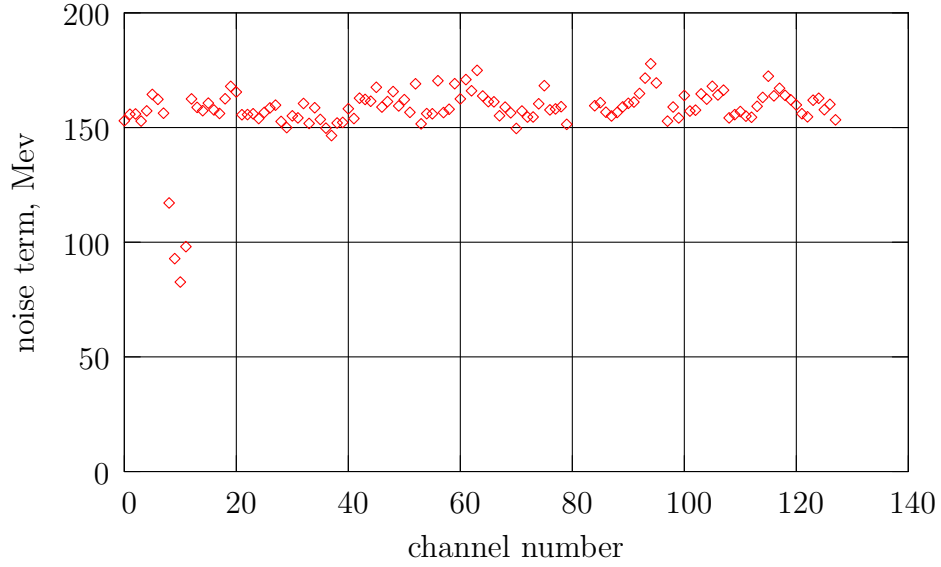
Figure 3.22. Noise term for low gain.

region $1.0 < |\eta| < 2.7$ and are arranged in four disks at 7, 10, 14 and 21-23 m from interaction region. There is an opening at $|\eta| = 0$ for the cables and services of the ID, the CSC and the calorimeters.

The main components of the muon chambers are MDT's. MDT consists of three to eight layers of drift tubes. A drift tube is an aluminum tube of 30 mm in diameter, operating with non-flammable gas mixture of 93% Ar and 7% CO_2 at 3 bar absolute pressure. The ionisation left by muon is collected by the central wire with a diameter 50 μm and at a potential of 3080 V. At the designed pressure MDT's provide 80 μm single-wire resolution and maximum drift time of 700 ns.

In the central region and large η regions Cathode Strip Chambers are used instead of the MDT's. The CSC is a multiwire proportional chamber with both cathodes segmented, one with strips perpendicular to the wires and the other parallel to them.
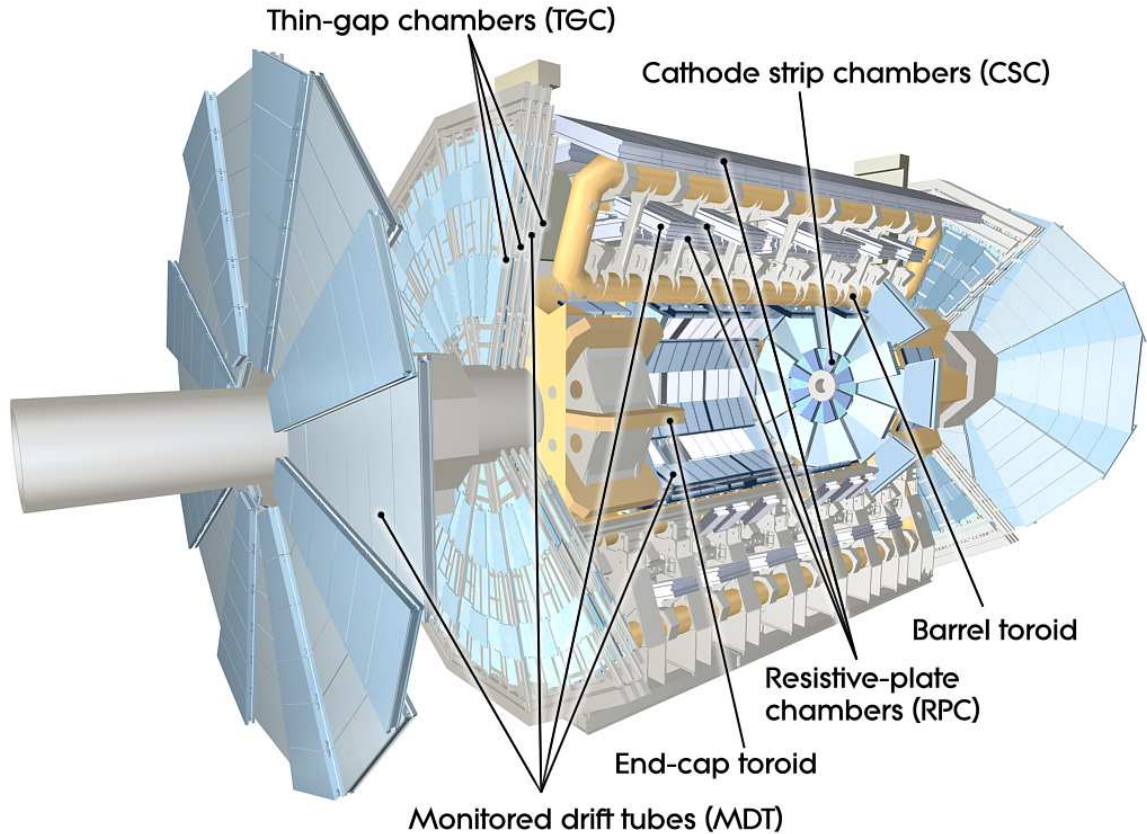
Figure 3.23. ATLAS Muon System.

The position of the track is obtained by interpolation between the charges induced on neighboring cathode strips. The CSC reaches a position resolution of 60 μm in bending direction and of 5 mm in non-bending direction. It also have small electron drift times (less then 40 ns) and good time resolution (about 7 ns).

The muon spectrometer is the largest subdetector in ATLAS and requires very precise mechanical accuracy of 30 μm. The problem is solved using a special optical alignment system providing monitoring of the dimensions and positions of the chambers and allowing to correct displacements up to 1 cm in offline analysis.

3.2.5. Trigger system.

At the LHC the collision rate is 40MHz for a bunch spacing of 25ns. The ATLAS trigger needs to reduce the incoming interaction rate to 200Hz, the rate that can be written to mass storage. Hence, it needs to provide a very efficient rejection of the high background rate online. At the same time, it needs to maintain an excellent and unbiased efficiency for rare signals as some important signatures have small cross sections and/or small branching ratios.

3.2.5.1. Level 1 trigger.

Level 1 (L1) is a hardware trigger based on coarse calorimeter and muon information. It searches for high p_T electrons/photons, muons, jets, hadronic τ-decays and large $\not{E}_T$. The bunch crossing rate of 40MHz has to be reduced to 100 KHz. During the decision time, the event information is stored in memory pipe-lines, located at the each detector read-out boards. The initial selection is based on the calorimeter and muon detector information. The L1 decision is made by Central Trigger Processor (CTP) that combine information for different object types.

The L1 Calorimeter Trigger (L1Calo) uses a Tower Builder Board (TBB) for EM calorimeter, that collects analog signals after the shaper (see Figure 3.8), sums them to build trigger towers, and transfers trigger towers to the Level 1 Receiver system. The analogous board for FCal and HEC do not do the summation and called tower-driver boards. This coarse information allows trigger system to find high energy deposition regions. The L1Calo aims to identify objects with high E_T, for example high p_T electron, events with large E_{Tmiss}, high p_T jets.

L1Calo is designed to work with about 7000 analogue trigger towers with granularity 0.1×0.1 in $\eta \times \phi$ from electromagnetic and hadron calorimeter. The first stage is digitization of the analogue input signals by pre-processor. Digital filter is

used to separate events from different bunch-crossing. Digitized data are transfered to the Cluster Processor (CP) and Jet/Energy-sum Processor (JEP) in parallel. The CP identifies electron, photon and τ candidates with E_T above programmable trigger threshold and certain isolation criteria, if required. The JEP identify jets and produce scalar and missing transverse energy, using 0.2×0.2 sums in $\eta \times \phi$.

If L1Calo accepts the event, the stored data are read out to DAQ system. This includes input data, intermediate calculations and trigger results. the types and positions of jets, τ-lepton and electromagnetic cluster candidates are also collected and sent to L2 trigger. The L1Calo information reach CTP in approximately 1,5 μs after the bunch-crossing.

The muon spectrometer has separate trigger chambers. It has Resistive Plate Chambers (RPC) in the barrel and Thin Gap Chambers (TGCs) in the end-cap regions.

The basic RPC is a typical gaseous ionization chamber with electric field of 4.5 kV/mm. The ionization electrons produced by high energy particle in the gas collected by the electric field and provide the current signal. There are three layers of RPC's located on both sides of the middle MDT's layer and inside the outer MDT station in the barrel. The TGC's have a similar design with CSC's, but their anode pitch is larger then the cathode-anode distance. There are three layers of TGP's located near middle MDT station. The muon trigger system provides fast and coarse information about muon tracks in the detector for high level triggers and allows bunch-crossing identification.

L1 muon trigger uses information from three layers of muon trigger chambers in barrel and end-caps, to identify a muon candidate. The trigger algorithm first search for a hit in the second RPC double plane. If it is found, the algorithm search for the hit in the first double layer within a road that is defined by the line connecting the

interaction point and the hit in the second layer. The width of the road is a function of the p_T cut. The higher the cut, the smaller the road. The requirement on the track is 3-out-of-4 hits in the first two double layers in low p_T algorithm. The high p_T algorithm also uses information from the third layer. It works the same way, finding at least one hit in the third double layer within the road. The center of the road is defined from low p_T algorithm, width depend on the p_T cut. The decision time for muon trigger is 2.1 μs.

The final decision is made by the CTP. It receives information from both calorimeter and muon triggers, compares it with programmable table of the trigger conditions (up to 256) and decides if the particular trigger is passed. Trigger conditions can be grouped in up to 256 trigger item, each condition can contribute to every trigger item.

3.2.5.2. Level 2 Trigger.

If event satisfies L1 trigger, the information is passed to level 2 (L2) trigger using 1574 Readout Links. L2 is a software trigger. 1574 event fragments are stored in 1574 Readout Buffers (ROB's). For every selected event L1 trigger system provides a Region of Interest (ROI) information. ROI is an $\eta \times \phi$ region near an interesting object detected by L1, for example high p_T electron or jet. Using ROI information one of the L2 supervisors (L2SV) selects what ROB should be read and what L2 trigger processing unit should analyze it. Selected ROB's are unpacked and particles in them are reconstructed using the normal reconstruction procedure. Thus, L2 trigger use normal reconstruction algorithms, but applies them only to the part of the event. The result of the analysis is also received by L2SV.

If the event is rejected by L2, it clears all ROB's. If event is passed, it is transferred to an event-building node (called SFI). The SFI collects information from all ROB's

and completely reconstructs the event. The full event is sent to the Event Filter (EF) for further analysis.

The L2 trigger reduces event rate from 100 KHz to 2.5 KHz, having decision time about 40 ms.

3.2.5.3. Event Filter.

The last trigger step Event Filter (EF) is also a software trigger. Using the reconstructed event from L2 EF check its own trigger conditions. The decision process for EF is the same as for L2, only full reconstructed event is used. If the event is passed EF classify it to a predetermined set of data streams and send to the output nodes (SFO's). The events received by an SFO are stored in the local file system.

The EF has a decision time 1 s and reduces the event rate from 2.5 KHz down to 200 Hz.

Chapter 4

TRIGGERING AND EVENT SAMPLES.

4.1. Monte Carlo Samples.

LHC and ATLAS will produce a complex signal. To be able to interpret evidence of a signal and to understand the backgrounds correctly, we need to simulate the detector and the physics processes. The only way to do it is to use "Monte Carlo data". Monte Carlo methods are a class of computational algorithms that rely on repeated random sampling to compute their results. These methods use existing theoretical models to describe behavior of the quantum particles. Random number generators allow to simulate the behavior of a given particle within the model. For example, in pp collisions the probability of a particular process is defined according to its theoretical cross section which weights the randomly generated probabilities. Simulated data are produced using several steps, including parton-level event generation, non-perturbative QCD evolution and detector simulation.

4.1.1. Event Generators.

During the first step, the specific physics process is simulated using special programs called "event generators". All particles in the event then undergo a chain of decays and fragmentation processes until only particles that can reach the detector ("final state particles") are left. After this step, we have complete information about all particles expected to be produced in the event just before they reach the detector.

In the ATLAS framework several particle generators are used. The most widely used one is called PYTHIA, [19]. The generator can simulate two colliding beams of different particles, including pp collisions that are needed for LHC. In general, two colliding particles have a scattering process. The probability of the process is given by its cross section that depends on the physics model used for its simulation. PYTHIA allows to choose one or more physics processes to model simultaneously. After the interaction, the produced particles have a series of decays until stable particles are produced. All colored objects go through hadronisation, producing colorless jets. The fragmentation is done according to the Lund string model (see section 1.1.2).

For supersymmetric processes, the generators ISAJET [30] and HERWIG [31] were used. ISAJET can simulate supersymmetric processes (this part of ISAJET even has a separate name ISASUSY). It allows setting masses of supersymmetric particles, so different regions of MSSM parameter space can be selected. Unfortunately, ISAJET uses only the most primitive Field-Feynman model for jet hadronisation. That is why HERWIG is used to perform soft QCD modeling. HERWIG uses a cluster model for jet hadronisation based on non-perturbative gluon splitting, and a similar cluster model for soft and underlying hadronic events. It takes into account soft gluon interference and azimuthal correlations within and between jets due to gluon interference and polarization. So, the combination of two event generators allows to get much more realistic picture of the event evolution.

4.1.2. Detector Simulation.

During the second step the effect of passing the stable particles from the event through the detector is simulated. After this step, the produced data are equivalent to the response of the ideal detector to the event. The information contains analog and digital signal values and so on. This step is usually done by a GEANT-based

66

program that knows the models of the underlying physics of the particle interactions in the detector.

The GEANT program describes the passage of elementary particles through matter [32]. Providing complete information of the detector structure to GEANT allows to simulate the passage of the particle through the detector, including signals generated in the subdetectors, energy loss in support structures and electronics, dead channels and so on. Calculationally, the program works similarly to the event generators. The model of the energy loss in a specific material is used to simulate passage through different regions. A random number generator is used to simulate different possible interactions in the detector.

4.1.3. Signal and Background Samples.

Considering the three lepton final state we are interested in, there are three physics backgrounds (producing three real leptons) and an instrumental background (one of the leptons is a jet fake). We have used simulation of these processes using 12.0.6 release. The samples, their cross sections and number of events used are summarized in Table 4.1.

Table 4.1. Monte Carlo samples and their cross sections that were used in the analysis

signature	number of events	cross section, fb^{-1}
SUSY	143000	7.3
$t\bar{t}$	382000	450
WZ	2500	0.3
$Zb\bar{b}$	37150	15
Z+jets, $Z \to ee$	43000	150
Z+jets, $Z \to \mu\mu$	47000	150

Let us look at the properties of the Monte Carlo generation of each sample more closely:

- *SUSY "SU1" (coannihilation) point:* This is inclusive sample, containing all possible decays, generated by ISASUSY+HERWIG.

- *top-anti-top ($t\bar{t}$):* $t\bar{t}$ sample with non all hadronic condition ($t\bar{t} \to \ell\nu X$). The condition means that at least one of the W's, produced in top decay, decays leptonically. The sample was generated using HERWIG.

- *WZ:* includes only $WZ \to \ell\ell\ell\nu$, generated by Jimmy.

- *Z+jets:* $Z \to e^+e^-$ or $Z \to \mu^+\mu^-$ together with two high p_T jets (jet p_T above 20 GeV). Generated by ALPGEN+HERWIG.

- *$Zb\bar{b}$:* $Zb\bar{b} \to \ell\ell\ell + X$, generated by PYTHIA.

The main problem with Monte Carlo data is that we produce the data according to our best knowledge of the process and the detector. The real detector and real physics may be different from our model. That is why the Monte-Carlo data need to be tested and scaled to correspond to the reality when the first data will be available.

4.2. Trigger and Data Acquisition.

In the real data taking process, only events that passed at least one of the triggers are stored. Thus, it is very important for the signal to pass at least one trigger. Also it is very important to know what triggers are triggered by every channel. Let us consider the possible trigger menu. Available data allowed to use only lepton triggers. In later releases more complicated trigger chains are available.

Because of the relatively low p_T lepton that are expected from coannihilation region, for the presented analysis, I considered triggers that are suitable for low p_T

leptons. Also $\not{E}_T$ is a standard feature of any SUSY decay chain because of two escaping LSP's, so I considered the only $\not{E}_T$ trigger available for my data.

- *EF_e10:* A single electron trigger at L1, L2 and EF. It starts with an electromagnetic cluster with $p_T > 5$ GeV at L1, and require an electron with $p_T > 10$ GeV at L2 and EF. No isolation is required.

- *EF_e15iEF_e15i:* Two electron trigger. Starts with two electromagnetic clusters with $p_T > 15$ GeV. At L1 no isolation is applied. Two isolated electrons with $p_T > 15$ GeV are require at L2 and EF. The isolation cut is based on the calorimeter information only.

- *EF_mu6:* Single muon trigger. Starts with single muon with $p_T > 6$ GeV at L1, L2 and EF. No isolation is required.

- *EF_met10:* $\not{E}_T$ trigger, loose selection. Starts with τ with $p_T > 5$ GeV at L1, $\not{E}_T > 10$ GeV at L2 and EF. This item is the only $\not{E}_T$ EF trigger available for the used data samples.

Table 4.2. Trigger efficiencies.

Trigger item	eee	$ee\mu$	$\mu\mu e$	$\mu\mu\mu$
EF_e10	1.000 ± 0.005	1.000 ± 0.003	1.000 ± 0.001	-
EF_e15iEF_e15i	0.792 ± 0.005	0.560 ± 0.003	-	-
EF_mu6	-	0.821 ± 0.003	0.963	0.98 ± 0.001
EF_met10	1.000 ± 0.001	1.000 ± 0.001	1.000 ± 0.001	1.000 ± 0.001

The final efficiencies at EF level are given in Table 4.2. As you can see, they are almost 100%. All or practically all signal events should pass atleast one trigger.

Chapter 5

EVENT RECONSTRUCTION AND PARTICLE IDENTIFICATION

The detector or Monte Carlo simulation provides us with a signal from each sub-detector. How can this information be converted into particle energy and momenta, missing energy and so on? This is done through the reconstruction process.

5.1. Track Reconstruction

Although, tracks are not used directly in my analysis, they are very important. The low p_T electron reconstruction rely on track reconstruction more then high p_T electron reconstruction. Tracking information is important for muon detection, especially for low p_T muons.

The inner detector allows reconstruction of charged particle tracks with $p_T >$ 0.5 GeV and $|\eta| < 2.5$ [22]. The raw data from pixel and SCT detectors is converted into "space-points", the points where tracks crossed the detector plane. A hit in a pixel detector or two hits from opposite sides of a SCT module give one space-point.

The track finding algorithm starts from finding track seeds (combinations of space-points in three pixel layers and the first SCT layer). The seeds are extrapolated through the SCT, providing track candidates. Then the candidates are fitted (using global χ^2 and Kalman fitters). Quality cuts are applied to remove fake tracks. The quality cuts include cuts on the total number of space-points, number of holes per track (a hole happens when the track crosses the detector layer leaving no signal). The selected tracks are extended into the TRT region. Finally, the extended tracks
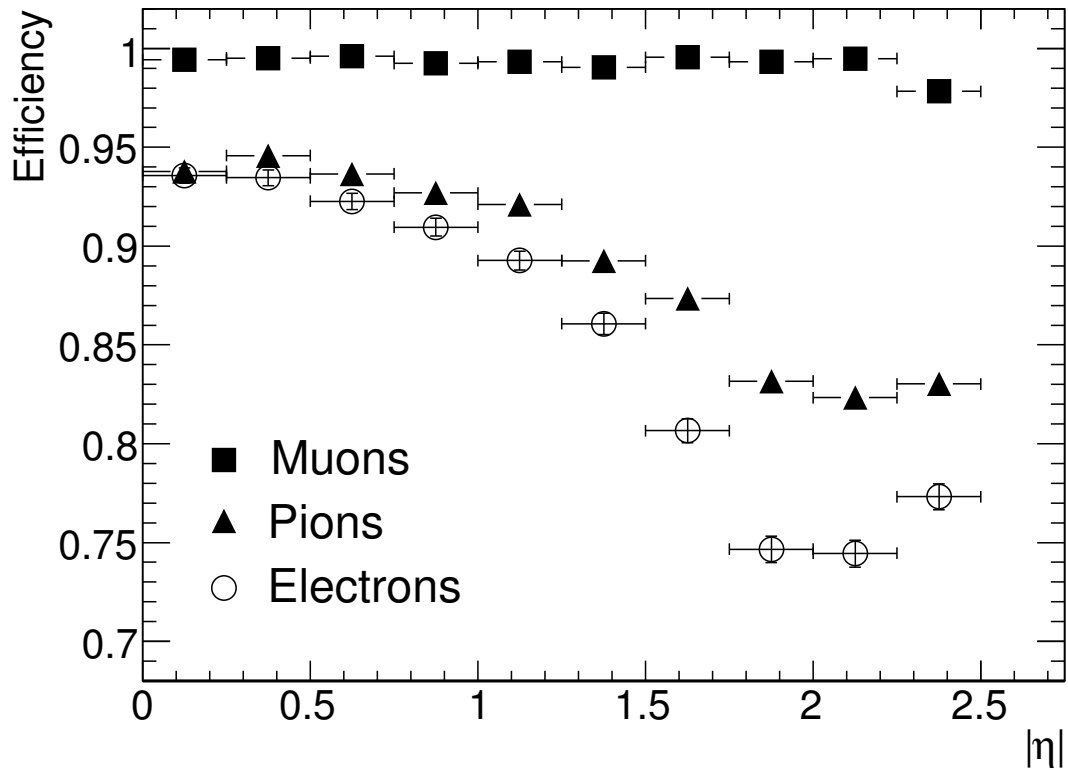
Figure 5.1. Track reconstruction efficiencies as a function of $|\eta|$ for muons, pions and electrons with p_T=5GeV. The inefficiencies for pions and electrons reflect the shape of the amount of material in the inner detector as a function of $|\eta|$.

are refitted using complete information from all three detectors. The standard cuts on reconstructed tracks are: 7 or more hits in pixel and SCT (one SCT space point is two hits), $|Z_0 \sin\theta| < 10\ mm$, $d_0 < 2\ mm$, where Z_0 and d_0 are distances from the track to the primary vertex in z and xy plane. The track reconstruction efficiency is shown in Figure 5.1.

After tracks are found, the primary and secondary vertices are reconstructed. For the primary vertex reconstruction all tracks are assumed to come from the same

vertex. The procedure takes several steps, removing tracks that are not coming from the common vertex (secondaries from interactions or decays of the lifetime particles) at each step. The resolution for the primary vertex finding gives 50 μm ix z direction and 20 μm in $x - y$ plane, depending on the number of tracks in the event.

5.2. Calorimeter Reconstruction.

To reconstruct the energy deposited in the calorimeter it must be calibrated [22],[24]. The first step, that converts the raw signal extracted from each cell (in ADC counts) into deposited energy is done by the readout electronics. This gives an energy, time and quality for each cell readout. The energy from several cells is combined into individual clusters corresponding to the total signal left by the particle in the calorimeter. As described in section 3.2.3.1, ATLAS electromagnetic calorimeter has four layers in depth. The total energy of the cluster is a sum of the energy deposited in each layer. It is calculated like

$$E = s(\eta)[c(\eta) + w_0(\eta)E_{PS} + E_{strips} + E_{middle} + w_3(\eta)E_{back}], \qquad (5.1)$$

where s is an overall scale factor, c is an offset, w_0 corrects for energy losses upstream of the presampler, and w_3 corrects for the longitudinal leakage, while E_{PS}, E_{strips}, E_{middle} and E_{back} are energies measured in the four calorimeter layers (presampler, strips, middle and back). The weights are determined using simulated single-particle events with energies from 5 to 200 GeV.

5.2.1. Electron Reconstruction

Real physics signal depends on the position where electron or photon hits the cell. The accordion shape of the cell makes these corrections small, they do not modify

the energy scale and usually have 1% from minimum to maximum for η- variations and 0.4 % from minimum to maximum for ϕ- variations. The overall position of the cluster is calculated using an energy weighted (η, ϕ) position in strips and middle layers. Then, the energy correction for specific η and ϕ is applied.
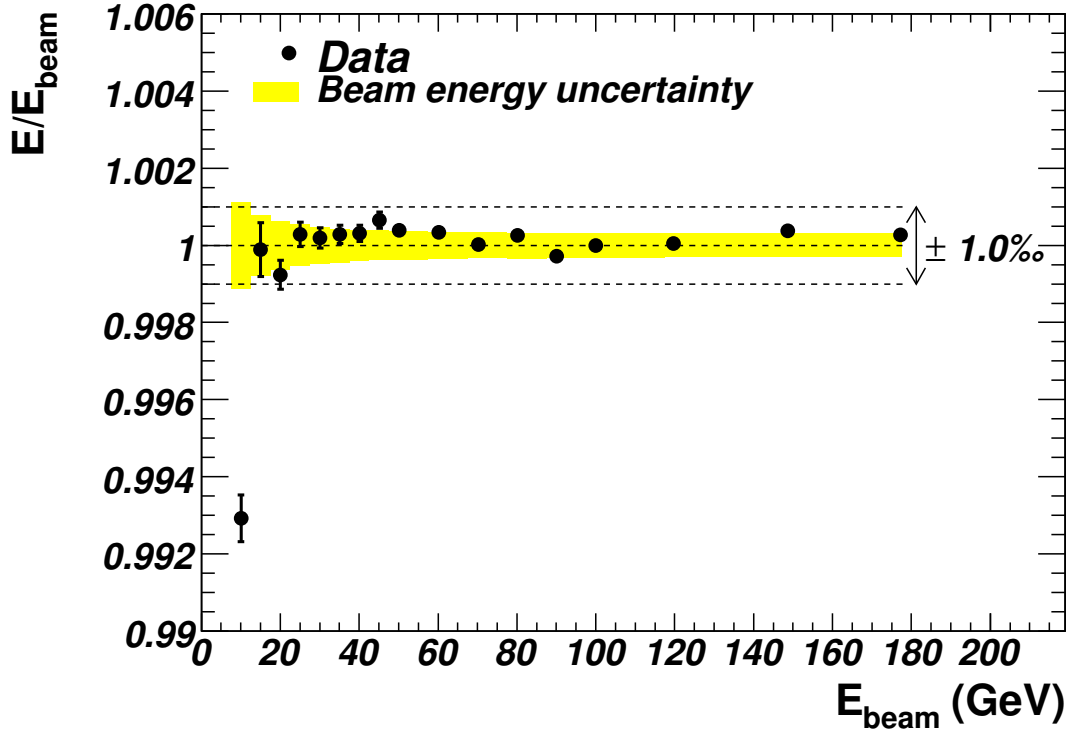
Figure 5.2. Linearity of calorimeter response as a function of the electron beam energy, E_{beam}, for a barrel LAr electromagnetic module at $|\eta|$=0.687. All points are normalized to the value measured at E_{beam}=100GeV. The total beam energy uncertainty is 1% and shown as a band.

The standard electron reconstruction algorithm starts from finding electron clusters in the calorimeter. The seed cluster is found by the sliding window algorithm. The window size is 5×5 calorimeter cells in the middle layer in η and ϕ. If the transverse energy in the window is greater then $E_T^{threshold}$=3 GeV, a fixed size cluster is

formed around the seed. The size of the fixed size cluster is 3×5 middle layer cells in the barrel and 5×5 layer 2 cells in the end caps. It gives an electron candidate if there is a loosely matched track, i.e. the track extrapolated to the calorimeter lies within 0.05×0.10 in $\Delta\eta \times \Delta\phi$ window. Also ratio E/p of the cluster energy to the track momentum should be less than 10. The linearity of the reconstructed energy depending on the beam energy is shown at Figure 5.2, the energy resolution as a function of energy is shown at Figure 5.3.

Figure 5.3. Expected relative energy resolution as a function of energy for electrons at $|\eta|$=0.3, 1.1, and 2.0. The curves are the fit lines.

Good electrons are selected from electron candidates using the cuts that are combined into three sets: loose, medium and tight [23].
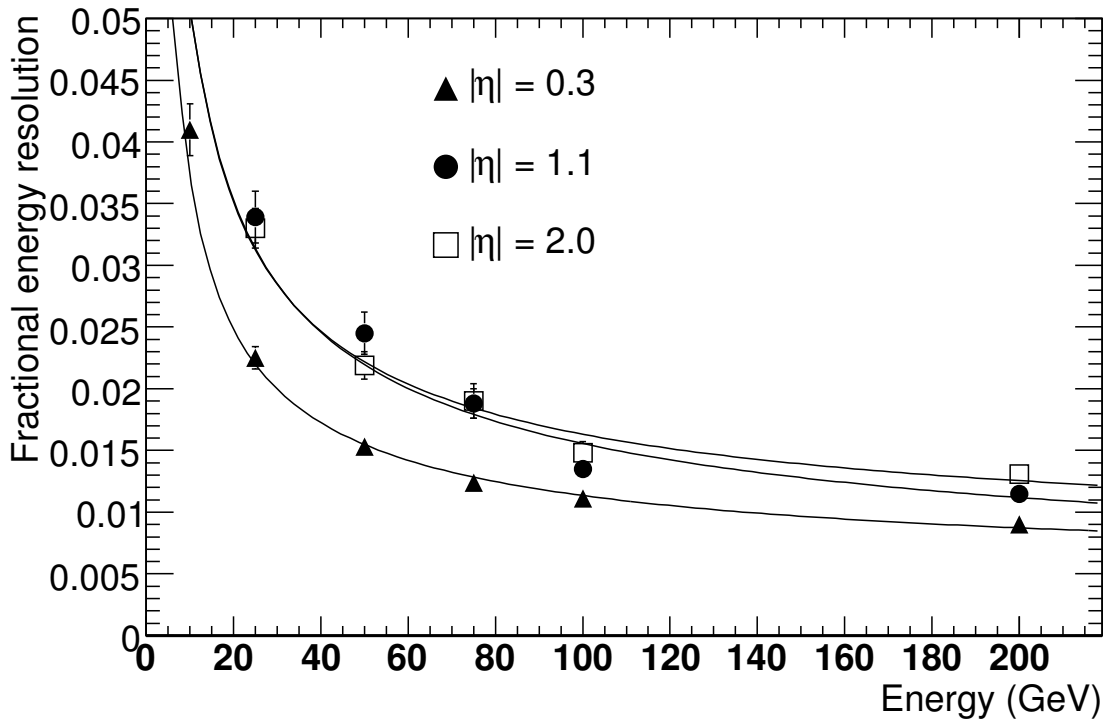
- ClusterHadronicLeakage - $\frac{E_T(firsthadronicsample)}{E_T(emcluster)}$; used in loose, medium and tight

- ClusterMiddleEratio37 - ratio of the cell energies in 3×3 versus 3×7; used in loose,medium and tight

- ClusterMiddleWidth - lateral width of the shower; used in loose, medium and tight

- ClusterStripsDeltaEmax2 - second largest energy deposit normalized to normalized to the cluster energy; used in medium and tight

- ClusterStripsDeltaE - difference between the second largest energy deposit and the smallest energy deposit; used in medium and tight

- ClusterStripsWtot - total shower width; used in medium and tight

- ClusterStripsFracm - energy outside core of the shower; used in medium and tight

- ClusterStripsWeta1c - width of the 3 strips around the maximum; used in medium and tight

- TrackPixel - Number of hits in the pixel layer (¿0); used in medium and tight

- TrackSi - Number of hits in the pixel and SCT (¿8); used in medium and tight

- TrackA0 - Transverse impact parameter (¡ 1 mm); used in medium and tight

The result of the passing these cuts are summarized in a 12 bit $IsEM$ flag. $IsEM$ = 0 is equivalent to tight; $IsEM$ 7 = 0 is equivalent to medium; $IsEM$ 2 = 0 is equivalent to loose. I used my own selection cuts that are slightly looser then medium ($IsEM$ 1f7 = 0, $IsEM$ < 3000). To select the ID cuts, I compared electrons that were born in interesting processes (produced in supersymmetric particles decays,

75

decays of $W^{\pm}$ and Z^0 bosons, τ-decays) with electrons that are born in jets using the truth information. Comparing values of the $IsEM$ variable for these two classes, I choose cuts that reject jet electrons and keep isolated ones. The results of medium cuts are compared with my ID selection in Table 5.1.

Table 5.1.   Comparison of standard ID cuts and my ID cuts for signal and backgrounds.

process	efficiency, medium cut	efficiency, my cut
signal	0.76	0.89
di-jet sample	0.13	0.16

5.2.2. Jet Reconstruction.

Hadronic showers or jets are found using calorimeter signals from both electromagnetic and hadron calorimeters. The jet finding algorithm can have two types of input: tower and topological cluster ("topo-cluster").

Towers are formed by collecting cells into a $d\phi \times d\eta$=0.1×0.1 regular grid. The tower signal is a sum of the signals from all cells included in the tower. If the cell is not completely included, because granularity is not an even devision of 0.1, part of the cell signal proportional to the area included in the tower is added. The towers with negative signal coming from noise are summed with adjacent towers until the signal is positive and can provide physical four-vector.

Topo-clusters reconstruct the three dimensional energy deposition of particles. The seed cell is a cell with energy $E_{cell} > 4\sigma_{cell}$, where σ_{cell} is the total noise (electronic and pile up). All neighbor cells are summed independently of their own signal. If a neighbor cell has $E_{cell} > 2\sigma_{cell}$, it is considered to be a secondary seed and its

76

neighbors are also included in the cluster. Finally, all surrounding cells above a very low threshold (typically above 0σ) are collected if there is no secondary seeds. This algorithm provides actual noise suppression, because cells with no signal are less likely to be included in the cluster.

Tower or topo-cluster signals are input to the jet finding algorithm. The seeded cone algorithm considers every particle in the cone of a certain size around the seed to be a jet. The seed must have $E_T > 1$ GeV (for tower or topo-cluster), cone size $R_{cone} = \sqrt{d\eta^2 + d\phi^2}$. The axis of the cone should coincide with the jet direction. The jet direction is calculated as the E_T-weighted centroid of the particles in the cone. For my studies, I used the fixed-cone algorithm with $R_{cone} = 0.4$ because the SUSY events have many jets. We can easily get two overlapping cones using this algorithm. these cones must be either merged or split. If two cones have no common towers, no merging is required. If two cones have common towers, then the decision is made based on the fraction of the transverse energy in the shared towers for the lower E_T cone. If $E_T^{shared}/E_T^{cone} > 0.5$, the two jets are considered as one and merged. Otherwise, the jets remain separate and each of the shared towers is included into the nearest jet in $\eta \times \phi$ space.

The output of the jet algorithm is an uncalibrated jet, i.e. its energy is at electromagnetic scale. To calibrate the jet energy, ATLAS detector uses a weighting function for each calorimeter cell that depends on the energy density (also known as H1 calibration). All calorimeter cells with four momentum (E_{cell}, p_{cell}) are resumed with weighting functions w, giving a new momentum

$$(E_{reco}, p_{reco}) = \Big(\sum_{N_{cells}} w(\rho, \bar{X})E(cell), \sum_{N_{cells}} w(\rho, \bar{X})p(cell) \Big) \qquad (5.2)$$
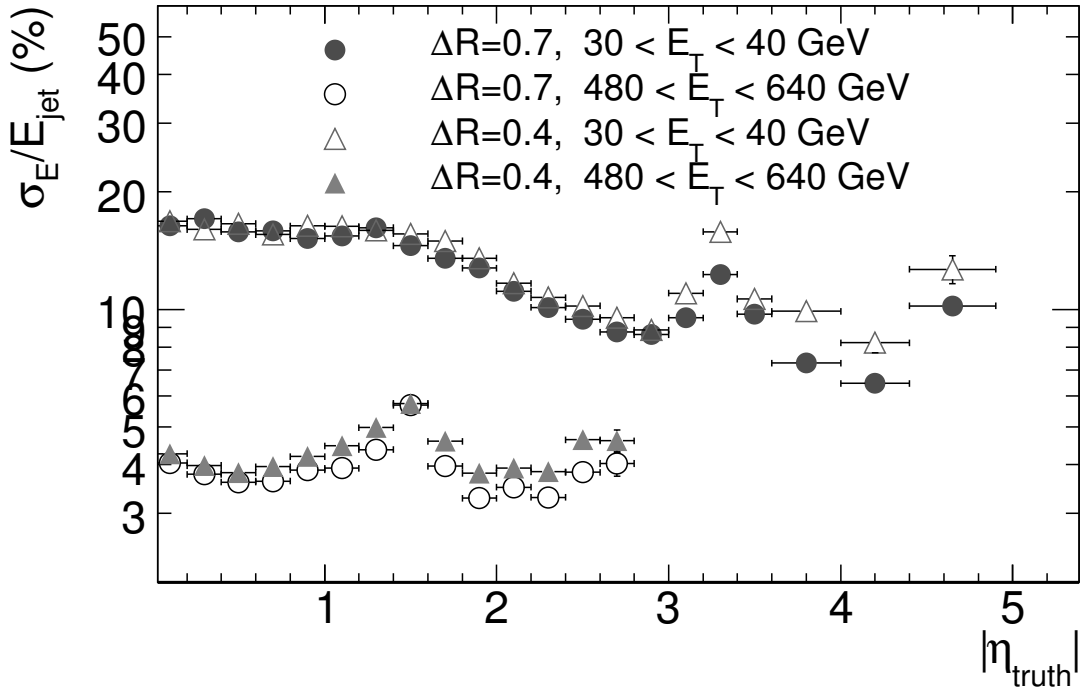
Figure 5.4. Jet energy resolution for QCD di-jets in two different E_T ranges, as a function of $|\eta|$ of the matched truth-particle jet. The results are shown for cone-tower jets with $R_{cone=0.7}$ and $R_{cone=0.4}$.

weighting functions w depend on the signal density, $\rho = E/V$ (V is volume), and position of the cell in the calorimeter, $\bar{X}$.

The weighting functions absorb all detector effects. The energy loss in inactive materials is implicitly included. The values of the weights are calculated using simulated QCD di-jet sample covering the whole p_T range expected at LHC. The final energy resolution for the fixed-cone algorithm is shown on Figure 5.4.

5.3. Muon Reconstruction

The muon reconstruction in ATLAS uses three strategies [22]. The first one relies on muon spectrometer only and is called "stand-alone". The second one is combination of the muon track with inner detector track. This is the combined strategy. And the third one is combination of the inner detector track with the segment from the muon spectrometer, i.e. track plus one of the inner muon stations.
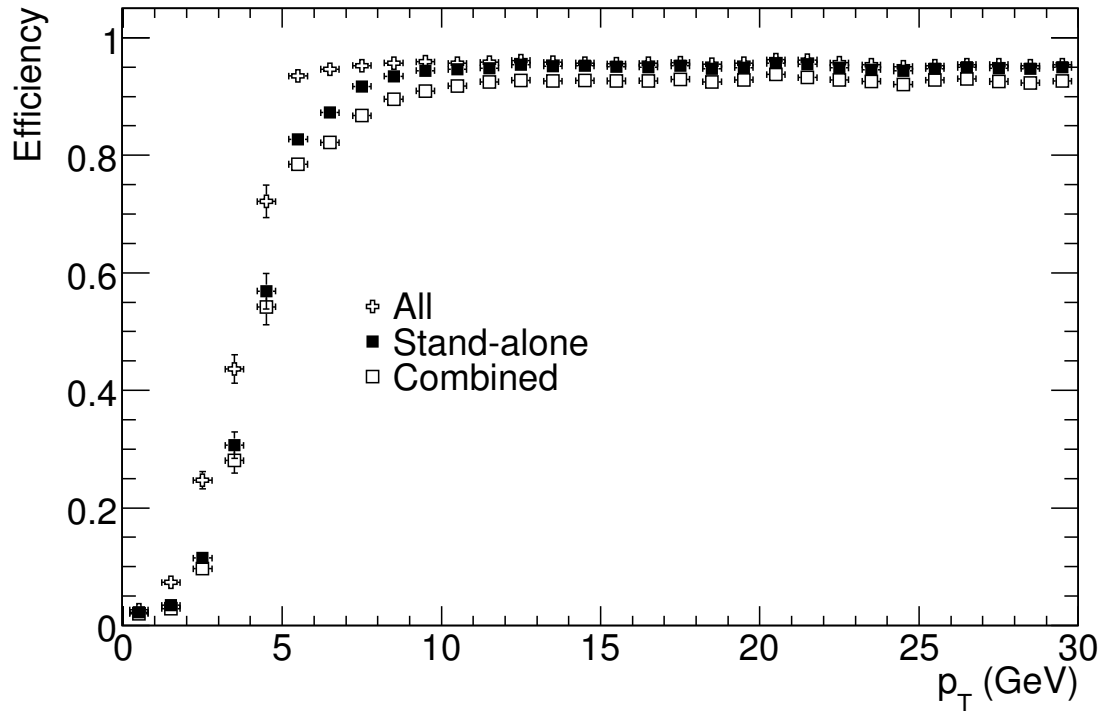

Figure 5.5. Efficiency for reconstructing muons as a function of p_T. The results are shown for stand-alone reconstruction, combined reconstruction and for the combination of these with the segment tags discussed in the text.

The reconstruction has several steps. During the first step raw data from MDT's and SCT's are processed. If the signal looks like signal from muon, the correspond-

ing line in the chamber is called track segment. The full muon track is built from segments, starting from the middle stations and extrapolating to the other regions. Then, for combined method, the muon spectrometer track is propagated in the inner detector, taking into account energy loss in the calorimeters. This allows much better performance for the muons with p_T less then 100 GeV.

In case of the segment tag method, the inner track is extrapolated in the inner muon stations. This method helps at the low p_T range, because muons below 6 GeV do not always reach middle and outer stations. In the barrel/end-cap transition region ($1.1 < |\eta| < 1.7$) the middle stations are missing for the initial data-taking. At the region η 0 muon acceptance is considerably lower.

5.3.1. Lepton isolation.

The signal has three isolated leptons while most of the backgrounds have at least one non-isolated one (look at Table 4.1 and end of Chapter 2 for a comparison of signal and backgrounds). For $t\bar{t}$ and $Zb\bar{b}$ backgrounds, the only way to get one of the leptons is to get it from the jet. It can be either a semileptonic b decay, when lepton is physically produced outside the jet, but very close to it, or a jet fake, where the jet mimics an electron signal. The jet fake rate is low (10^{-4}), but leptons from b decay are produced rather often (in 0.17 of all b decays for e and μ separately).

If a lepton is produced in a jet, the nearest space around it should contain some hadronic signal from the remnant of the jet. The way to distinguish such a lepton is by isolation. The standard isolation variable is a transverse energy in a certain cone around the direction of the particle, minus the transverse energy of the particle itself. It is called "etcone" and is calculated for a set of different cone sizes. The standard isolation cut is $etcone(dR < 0.2) < 10$) GeV is not very efficient. From the Table 5.2 you can see that standard isolation gives almost no rejection compare

Figure 5.6. Isolation efficiency and fake rate for electrons. The dashed curves are for the standard isolation variable, the solid curves are for the $\frac{etcone(R)}{E_T(lepton)}$. Blue curves are for $dR < 0.2$, red curves are for $dR < 0.3$, green curves are for $dR < 0.4$

to the ID cuts. I found that $\frac{etcone(R)}{E_T(lepton)}$ is more efficient cut. On the Figures 5.6 and 5.7 you can see efficiencies of the different isolation cuts for the signal versus fake rate of the $t\bar{t}$ background. The chosen cuts, $\frac{etcone(R<0.30)}{E_T(electron)} < 0.16$ and $\frac{etcone(R<0.20)}{E_T(muon)} < 0.14$, provide 0.86 efficiency for electrons, 0.91 efficiency for muons and 0.10 fake rate for both. From Table 5.2 it is clear that, after combining ID and isolation cuts, my cuts are more efficient then the standard ones. They provide approximately the same efficiency for the signal, but gave a large gain in fake electron rejection.
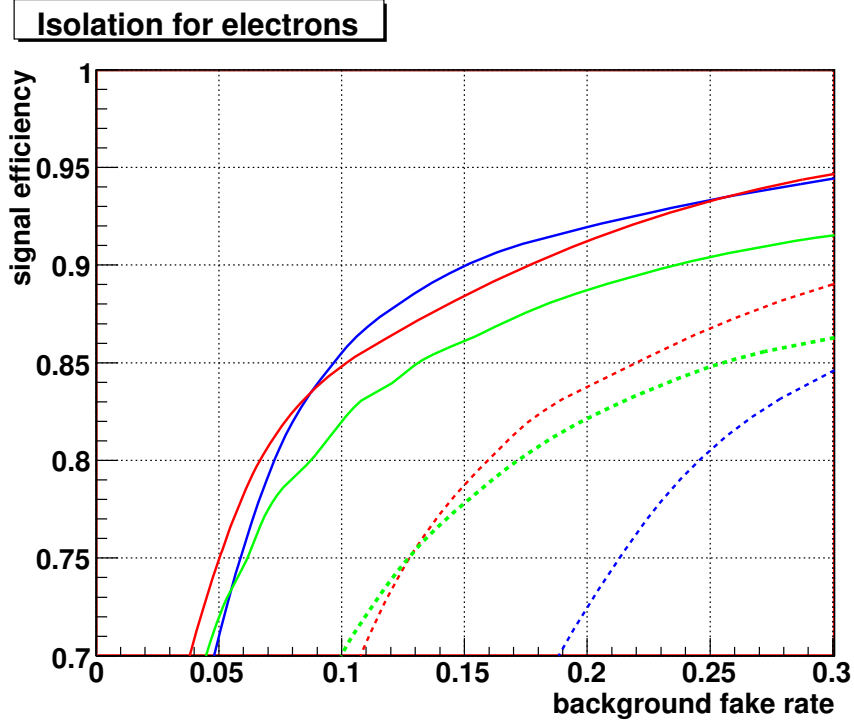
81
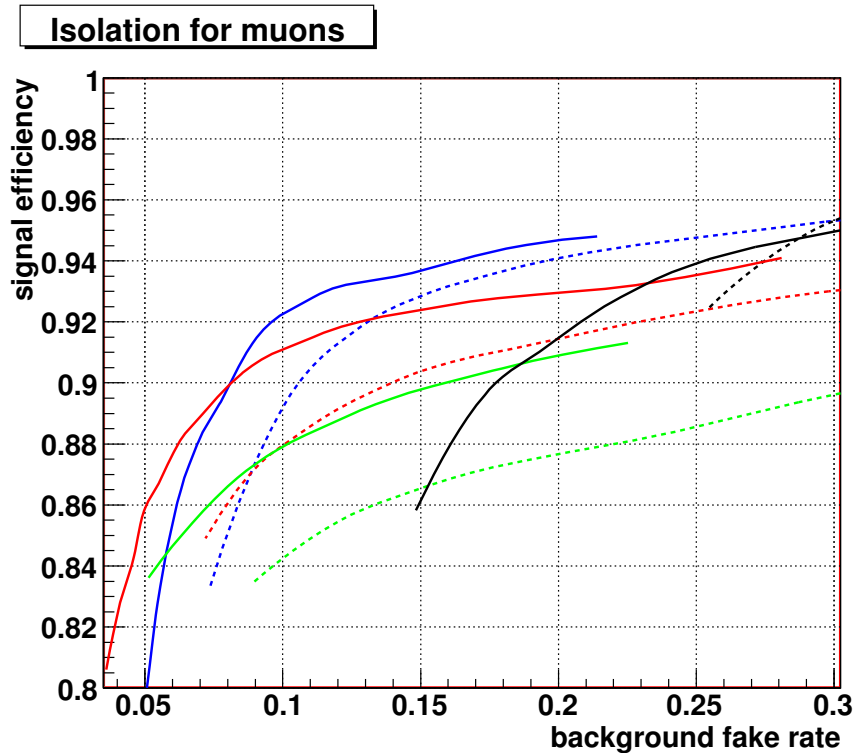
Figure 5.7. Isolation efficiency and fake rate for muons . The dashed curves are for the standard isolation variable, the solid curves are for the $\frac{etcone(R)}{E_T(lepton)}$. Black curves are for $dR < 0.1$, blue curves are for $dR < 0.2$, red curves are for $dR < 0.3$, green curves are for $dR < 0.4$

5.3.2. Missing Transverse Energy Reconstruction.

In pp collision the total p_T of incoming particles is 0, so total p_T of all decay product should be 0 as well. If the net observed total p_T of outgoing particles is not 0, then some of them must escape the detector, for example $\nu's$. Knowing the total p_T of the observed particles and jets we can calculate the missing one. The transverse energy that is carried away by non-observable particles is called "missing transverse energy". The $\not{E}_T$ reconstruction is very important for any supersymmetric

Table 5.2.   Comparison of standard ID and isolation cuts with mine. The data are calculated relative to the number of electron candidates without any cuts.

process	efficiency, medium cut	efficiency, medium cut + standard isolation	efficiency, my cut	efficiency, my cut + my isolation
signal	0.76	0.73	0.89	0.75
di-jet sample	0.13	0.13	0.16	0.002

signal because two LSP's escape the detector, and provide large $\not{E}_T$.

The first step of the $\not{E}_T$ reconstruction in ATLAS is based on the calorimeter cell energies (after calibration) and reconstructed muons. The muon term is calculated using the stand-alone muon reconstruction. Muon energy loss in the calorimeter is not double counted this way and enters the calorimeter term. Only good muons with a matching track are considered, reducing the impact of the muon fakes.

The second step takes into account the cryostat term. It corrects the energy loss in the cryostat between the LAr electromagnetic and tile calorimeters.

The final step is a refined calibration of the $\not{E}_T$. Each high p_T object in the event is associated with the global calibrated cells. Starting in a carefully chosen order, electrons, photons, hadronically decayed τ's, b-jets, light jets and muons, replace contribution from the calorimeter cells. Now, instead of the energy and position of the calorimeter clusters, we have energy and position of corresponding particles and jets. The cells that survive the noise cut, but are not associated with high p_T objects also included. Then, final $\not{E}_T$ is calculated. Its resolution is shown on the Figure 5.8.
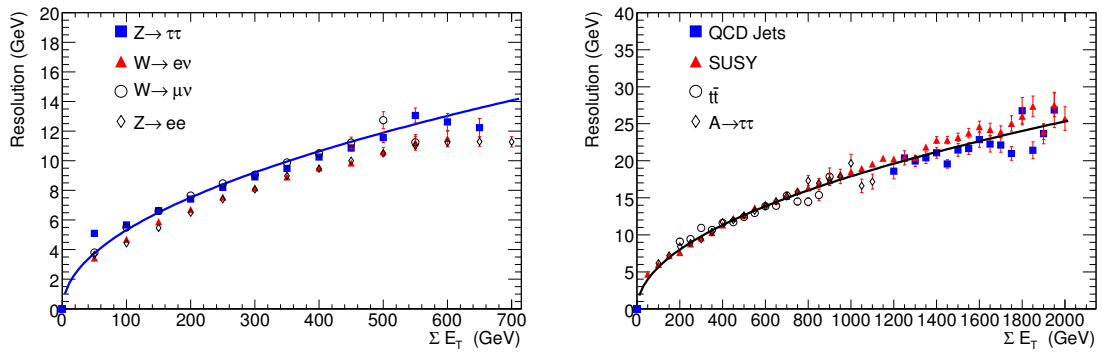
Figure 5.8. Resolution σ of the $\not{E}_T$ vector for low-medium values (left) and for low to high values (right). Different physics processes were used to be able to cover the whole $\not{E}_T$ range.

84

Chapter 6

KINEMATIC EVENT SELECTION

6.1. Kinematic Distributions and Preselection

The difference between signal and background signatures are shown in Table 4.1 in the Chapter 4. The lepton p_T distributions are shown in Figure 6.1. Two leading leptons for all backgrounds are produced in W or Z decays. They must have relatively large p_T 50 GeV. The third lepton is either born in b-jet for $t\bar{t}$ and $Zb\bar{b}$ or a jet fake for $Z+jets$. Semileptonic b-decay produces a low p_T lepton, the jet fake rate is larger for small p_T jets, so in both cases the third lepton is soft. The WZ produces three high p_T leptons, but its cross section is small. That is exactly what we can see in Figure 6.1 for the backgrounds. For the signal, the leptons come from χ_2^0 or $\chi_1^\pm$ decays. In coannihilation region, one of the leptons from χ_2^0 is soft, because the mass difference between initial and final particles is 10 GeV. Two leading lepton have the p_T's in the same range as the leading leptons from backgrounds. Thus, the distribution of the lepton p_T's are similar for the signal and backgrounds.

SUSY events have from 2 to 4 high p_T jets related produced in $\tilde{g} \rightarrow \tilde{q}$ and $\tilde{q} \rightarrow q$ decays. These jets are higher in p_T than QCD jets, so the signal must have at least two high p_T jets. Jet activity in $t\bar{t}$ is also relatively high, because it contains two high p_T b-jets from t decays and might have extra jets from hadronic W decays. The average number of jets in signal and $t\bar{t}$ events is ~ 6. $Zb\bar{b}$ background also has two b-jets, but the total number of jets in the event is lower, ~ 4. WZ sample has small jet
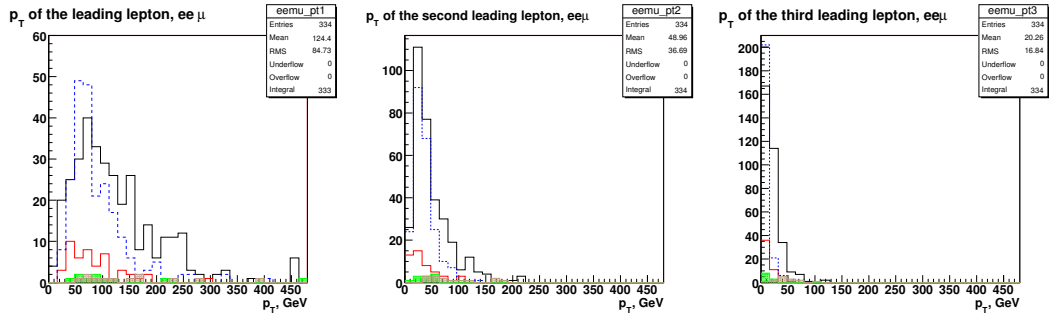
Figure 6.1. p_T's of the leading lepton(top left), the second leading lepton (top right) an the third leading lepton (bottom) for the signal and backgrounds. Black line is for SUSY, red one for $t\bar{t}$, dashed blue line is for $Zb\bar{b}$, green filled histogram is for WZ, brown filled histogram is for Zb+jets.

activity (jets per event) and low jet p_T. $Z+jets$ sample has a production requirement of two jets with p_T >20 GeV, but other jets are low p_T QCD ones. Thus, the signal has more energetic jets than the backgrounds. The p_T distribution of the two leading jets is shown in Figure 6.2.

$\not{E}_T$ is large for SUSY, because of two LSP's that escape the detector. It is also large at $t\bar{t}$, because of neutrinos from W decays. WZ, $Z + jets$ and $Zb\bar{b}$ have small $\not{E}_T$, originating from jets. The $\not{E}_T$ is shown in Figure 6.3 on the left.

To select a simple and non-biased signal signature with the maximum efficiency it was decided to use following cuts: three isolated leptons with p_T > 5 GeV (the main backgrounds have at least one non isolated lepton) and two jets with p_T > 40 GeV (high efficiency (∼90 %) for the signal). These are event preselection cuts. The effect of different cuts on number of events is shown in Table 6.1. The preselection cuts allow us to be sure that main characteristic of the signal are in the selected event (except for $\not{E}_T$) and at the same time leave a lot of space for further selection during
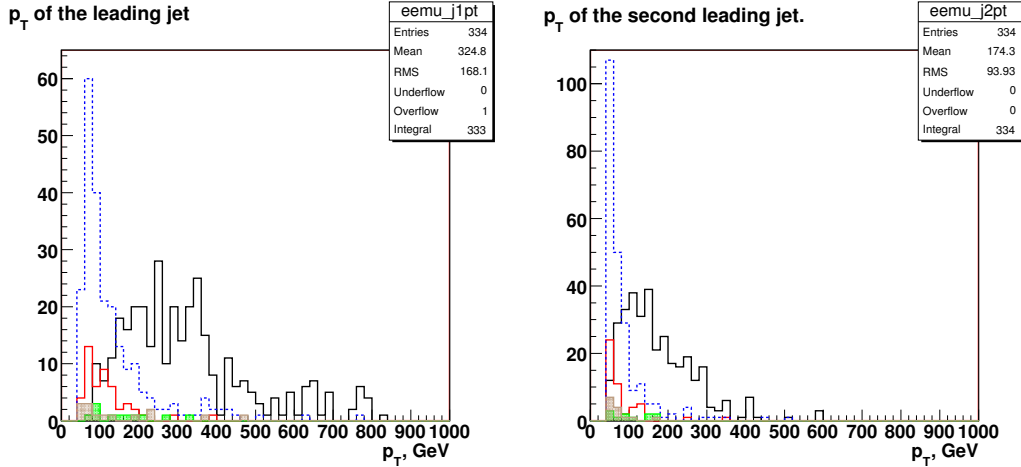
Figure 6.2. p_T's of the leading jet (left) and the second leading jet (right) for the signal and backgrounds. Black line is for SUSY, red one for $t\bar{t}$, dashed blue line is for $Zb\bar{b}$, green filled histogram is for WZ, brown filled histogram is for Zb+jets.

the optimization procedure.

6.2. Optimization of Kinematic Selection

The current analysis is done for the early discovery possibility. That is why all the values of the cuts are selected to maximize the search sensitivity. To estimate the discovery potential a statistical significance parameter,

$$\rho = \frac{S}{\sqrt{S+B}}, \tag{6.1}$$

is used. Under the assumption that the search is limited by statistics, not systematic uncertainties, the figure should be reasonably correlated with the significance measured in the actual experiment. A significance of 5σ is considered sufficient for a discovery.

Table 6.1. Number of events in 1 fb^{-1} for the signal and backgrounds with different cuts applied

Process	$3l$ p_T > 5 GeV	+isolation	+2 jets p_T > 5 GeV
$SUSY$	800	80	72.9
$t\bar{t}$	23000	800	377
$Zb\bar{b}$	16000	4200	1453.6
WZ	132	80	11.6
$Z + jets$	1056	152	159

The main goal of the signal selection optimization is to find a set of cuts that will maximize significance. An obvious variable candidate is $\not{E}_T$. The distribution for signal and backgrounds is different (see Figure 6.3) and $\not{E}_T$ cut was not used at the preselection level. The difference in jet activity should be taken into account. Instead of p_T's of two leading jets that have been used for preselection, I decided to use a combined variable H_T

$$H_T = \sum_{alljets} E_T(jet). \tag{6.2}$$

I tried sum of two leading jets only and the sum over all jets in the event. The latter choice is better because it takes into account the fact that SUSY events have more jets than WZ and $Zb\bar{b}$ events and might have more than two high p_T SUSY jets.

H_T distribution is in Figure 6.3 on the right plot. A minimal 5 GeV cut is low for electron and muon reconstruction and raises question if the fake rate is under control. Its potential to impact the significance should be studied. These reasons provide five optimization variables: $\not{E}_T$ and H_T, 3 lepton p_T's.
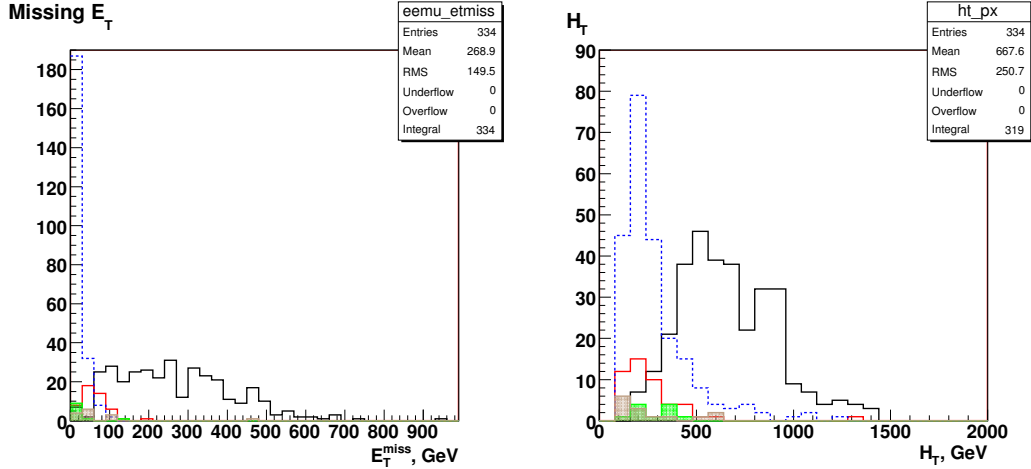
Figure 6.3. $\not{E}_T$ (left) and H_T (right) distributions for the signal and backgrounds. Black line is for SUSY, red one for $t\bar{t}$, dashed blue line is for $Zb\bar{b}$, green filled histogram is for WZ, brown filled histogram is for Zb+jets.

To check how the significance depends on these variables a grid search has been done. Extra cuts with varying thresholds were applied after preselection cuts. The $\not{E}_T$ threshold has a range from 0 to 460 GeV with step size 20 GeV. The H_T thresholds varied from 0 to 1000 GeV with step size 50 GeV. All three lepton p_T cut limits change from 5 to 14 GeV with the step size 1 GeV. For each point of the grid the significance was calculated. This allows to find the maximum and to check the dependence on different variables.

6.2.1. Optimization in $\not{E}_T$ and H_T

We investigated each of the four channels by grid searching in the $\not{E}_T$ vs. H_T plane. Preselection cuts were applied. The significance dependence for each channel separately is shown at Figure 6.4. x-axis is cut on H_T, y-axis is cut on $\not{E}_T$, z-axis is significance ρ. The plot is smoothed between grid points. It is evident that all
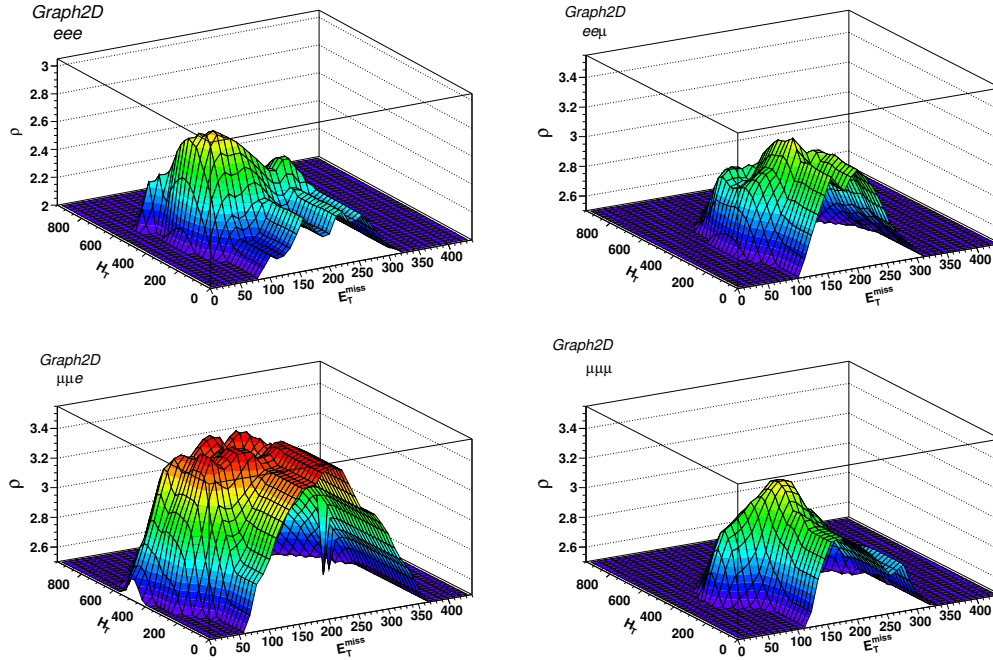
Figure 6.4. Optimization in $\not{E}_T$ and H_T, each channel separately, p_T of all leptons above 5 GeV. Step size is 50 for H_T and 20 for $\not{E}_T$. Top left plot is for eee, top right for $ee\mu$, bottom left for $\mu\mu e$ ans bottom right for $\mu\mu\mu$ channels.

channels have a similar behavior, obtaining $\rho = 3.0 - 3.6$. The positions of the maxima are given in Table 6.2.

6.2.2. Optimization of Lepton p_T's Selection.

Now, let us check how significance depends on lepton p_T. $\not{E}_T$ and H_T cuts are set to be at the values from Table 6.2, events from all channels are grouped together. All cuts on lepton p_T's range from 5 to 14 GeV. The result is shown at Figure 6.5. x- and y-axis are cuts on lepton p_T's, z-axis is significance ρ. The significance has almost no dependence on the leading lepton p_T in the given range, the dependence

Table 6.2. Cut values that provide maximum significance for each channel separately. All three leptons have $p_T > 5$ GeV, luminosity 1 fb^{-1}.

channel	$E_T miss$	H_T	$max(\rho)$
eee	> 100	> 350	3.0
$ee\mu$	> 160	> 250	3.3
$\mu\mu e$	> 140	> 300	3.6
$\mu\mu\mu$	> 160	> 350	3.3
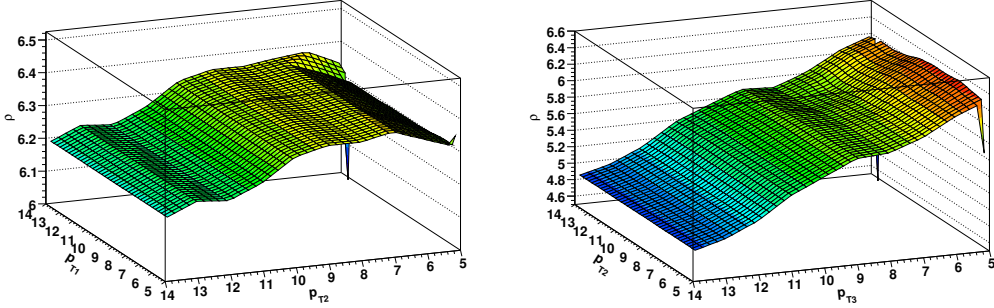
Figure 6.5. Optimization on lepton p_T using p_T's of two leading leptons on the left and p_T's of the second and third leading leptons on the right.

on the second lepton p_T is not very strong up to 9-10 GeV, but the lowest p_T lepton is rather sensitive. From this result, we conclude that the lepton cuts will be 10, 7 and 5 GeV.

6.2.3. Final Optimization.

The lepton p_T cuts are changed in the previous section, so we need to make a grid search in the $\not{E}_T$ vs. H_T plane again. Because of the similarity of the cuts in Table 6.2 the $\not{E}_T$ and H_T were changed simultaneously for all channels.
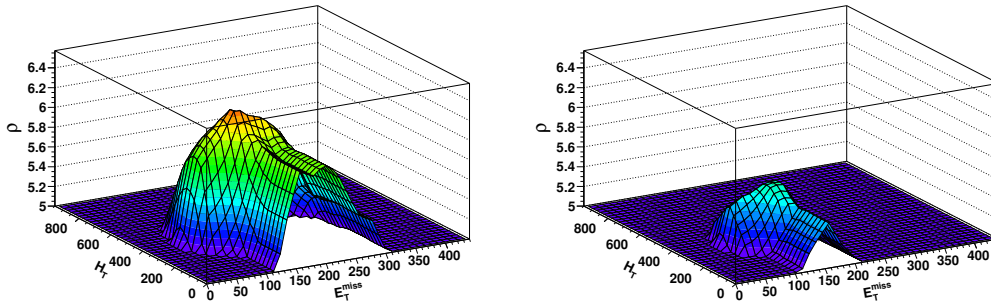
Figure 6.6. Optimization in $\not{E}_T$ and H_T, $p_{T1} > 10$ GeV, $p_{T2} > 7$ GeV, $p_{T3} > 5$ GeV (left) and optimization in $\not{E}_T$ and H_T, $p_{T1,2,3} > 10$ GeV (right).

The final optimization plot for all four channels is given in 6.6. The events from all four channels were summed and then the significance was calculated for two sets of cuts given in Table 6.3.

Table 6.3. Final cuts and significance in 1 fb^{-1}.

p_{T1}	p_{T2}	p_{T3}	H_T	$\not{E}_T$	ρ
> 10 GeV	> 7 GeV	> 5 GeV	> 350 GeV	> 140 GeV	6.4
> 10 GeV	> 10 GeV	> 10 GeV	> 350 GeV	> 140 GeV	5.6

The maximum significance is 6.4, it is well above the discovery limit. If three leptons have $p_T > 5$ GeV, there is a drop in significance down to 5.6. The number of events for preselection and final cuts are shown in Table 6.4.

92

Table 6.4. Number of events after final cuts with statistical errors

process	N_{events} preselection cuts	N_{events} final cuts
$SUSY$	73 ± 9	57.1 ± 1.7
$t\bar{t}$	377 ± 19	17 ± 5
WZ	12 ± 3	0.15 ± 0.15
$Zb\bar{b}$	$(1.45 \pm 0.04)10^3$	6 ± 3
$Z + jets$	189 ± 14	3 ± 3
$all\ BG's$	$(2.03 \pm 5)10^3$	26 ± 7
$significance$	1.6 ± 0.2	6.4 ± 0.6

Chapter 7

EXPECTED SENSITIVITY

While we expect significance ρ to be correlated with the observed significance in the real experiment, it is not a true sensitivity of a real experiment. The real detector has features that are not included in Monte-Carlo simulation. Some of the systematic effects cannot be modeled. Also, statistics for signal and especially backgrounds is low and not Gaussian, but Poisson.
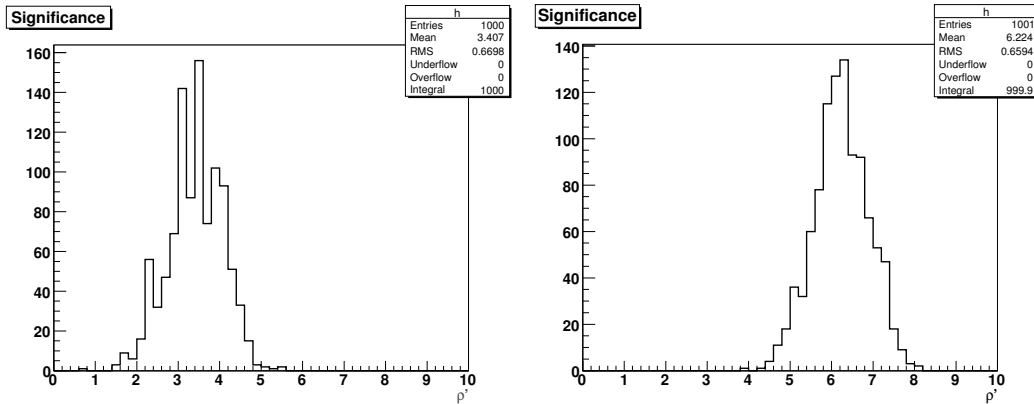
7.1. Ensemble Testing.

Figure 7.1. Sensitivity for 1 fb^{-1} (right) and 0.3 fb^{-1} (left).

To properly account for statistical fluctuations, we need to make many pseudo-experiments ("ensembles"). The ensemble is an estimate of the number of events for the signal and backgrounds using random values that have Poisson distribution

94
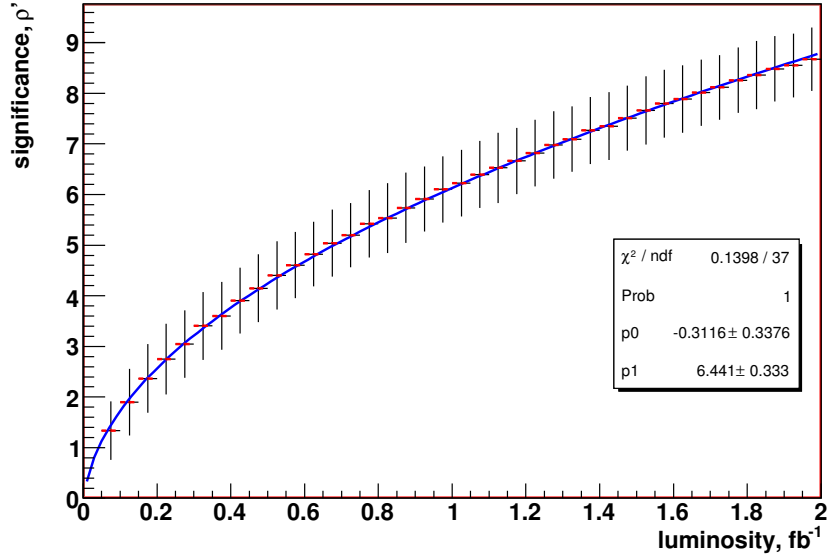
Figure 7.2. Significance versus luminosity, for luminosity changing from 0 to 2 fb^{-1}. The data are fitted by function $p1\sqrt{x} + p0$ (blue line). The data points are shown with rms bars (black) and error bars (red).

with mean equal to the number of events found in Chapter 6 (see Table **??**). These data are used to calculate the significance ρ' for each ensemble. The significance was calculated as

$$\rho' = \frac{N_{SUSY} + N_{t\bar{t}} + N_{WZ} + N_{Zb\bar{b}} + N_{Z+jets} - \langle N_{BG} \rangle}{\sqrt{N_{SUSY} + N_{t\bar{t}+N_{WZ}+N_{Zb\bar{b}}+N_{Z+jets}}}}, \qquad (7.1)$$

where $\langle N_{BG} \rangle$ is an average number of events for all background channels for each ensemble.

Table 7.1. Event yields and significance for several luminosity values.

luminosity, pb^{-1}	Number of signal events	Number of BG events	$\langle \rho' \rangle$	S/B
300	17	8.4	3.4	2.04
500	28	14	4.4	2.04
1000	57	28	6.2	2.04
2000	114	56	8.8	2.04

A range of luminosities was tried from 100 pb^{-1} to 2 fb^{-1}. For each luminosity 1000 ensembles were tried and ρ' was calculated. Figure 7.1 shows an example of the distribution when luminosity is 0.3 fb^{-1} (mean value is 3.41 and RMS is 0.67) and 1 fb^{-1} (mean value is 6.25 and RMS is 0.63).

Also, the interesting question is how the significance changes with luminosity. To do that I did the statistical analysis for 40 different luminosity points 1000 ensembles at each point. The number of events were scaled from Table ?? to represent luminosity from 0 to 2 fb^{-1} with a step size 50 pb^{-1}. The significance at each luminosity point is a mean value calculated over 1000 ensembles. This is an estimate of the typical statistical sensitivity for the range of luminosity. The resultant curve and a fit are shown at Figure 7.2. Using the fit parameters we can state that significance depends on the luminosity as:

$$\rho' = (6.4 \pm 0.3)\sqrt{luminosity} - (0.03 \pm 0.03) \tag{7.2}$$

The values of the significance and numbers of signal and total background events for several luminosity points are shown in Table 7.1. The number of events is scaled from 1 fb^{-1} data, the significance is ρ' averaged over 1000 ensembles. The discovery

limit $\rho' = 5$ is reached at 650 pb^{-1}.

7.2. Calibration Uncertainty.

Table 7.2. Number of events for signal and backgrounds with and without shift in jet energy

process	N_{events} shift up	N_{events} without shift	N_{events} shift down
$SUSY$	58.3	57.1	55.3
$t\bar{t}$	21	17	17
WZ	0.44	0.15	0.15
$Zb\bar{b}$	6	6	6
$Z + jets$	3	3	3
$all\ BG's$	30	26	26

These results and results in Chapter 6, depend largely on the quality of calibration, particularly of jets. The uncertainty in the jet energy scale early in the run will likely be large. This also impacts the $\not{E}_T$. So, this can cause the greatest uncertainty in the significance. To account for this, I have done an artificial shift in the jet energy scale up and down by10 % and checked the effect on the result. The results are summarised in Table 7.2, showing how the shift in jet energy scale affects the number of events for signal and backgrounds.

The fit on the significance versus luminosity distribution for up and down cases is shown at Figure 7.3. The number of events and its errors for signal and backgrounds are shown at Table 7.3.
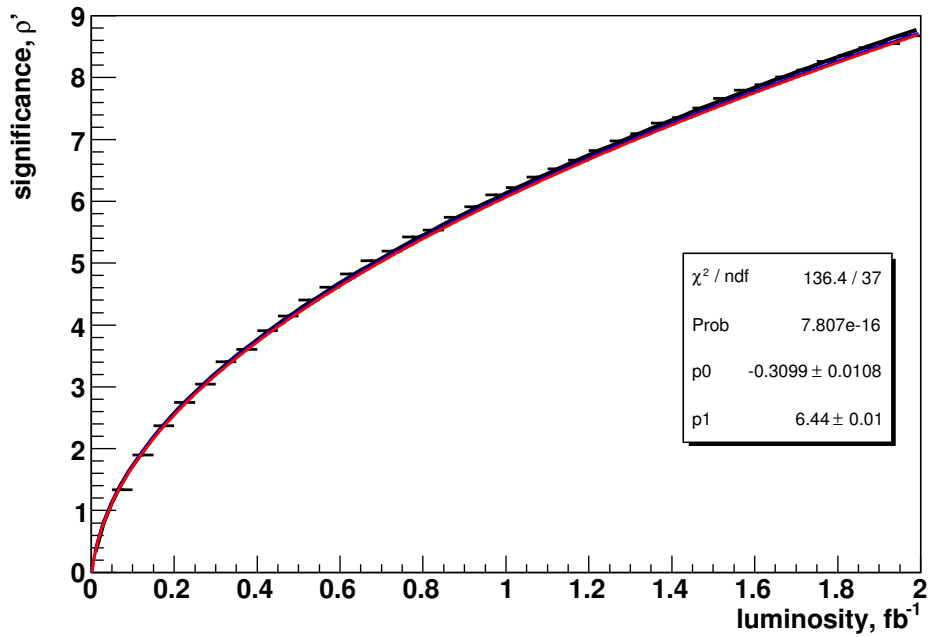
Figure 7.3. Significance versus luminosity for the original data plus three fit lines for the original data (black), with jet scale shifted up (blue) and down (red).

Table 7.3. Number of events after final cuts with statistical and systematic errors

process	N_{events} final cuts	σ_{stat}	σ_{syst}
$SUSY$	57.1	1.7	+1.3/-1.7
$t\bar{t}$	17.	5	+3.5/-0
WZ	0.15	0.15	+0.29/-0
$Zb\bar{b}$	6	3	+0/-0
$Z + jets$	3	3	+0/-0
$allBG's$	26	6	+3.5/-0

98

Chapter 8

CONCLUSION

The purpose of this thesis is to show a possibility of SUSY discovery at low luminosity in the coannihilation region using three lepton signal. The presented results show that the discovery is possible in 1 fb^{-1}, the significance of the SUSY signal is 6.4. The analysis was done using Monte Carlo data, the possible backgrounds include $t\bar{t}$, $Zb\bar{b}$, WZ, and Z+jets processes.

An electron reconstruction is very important for the presented search, so the work done during the Front End Crate Test is also presented. During the FECT the whole readout chain of LAr calorimeter was tested, including the calibration with calibration board and Optimal Filtering Coefficients calculation.

The search in the coannihilation region involves low p_T leptons. The performance of the ATLAS detector for such search, especially for low p_T electrons need more study. The standard lepton ID is not very efficient and need improvement. This includes the isolation implementation.

The SUSY discovery does not give us much information about particular SUSY model. To be able to find what supersymmetric scenario is realized in nature we need information about masses of the supersymmetric particles and their properties. Masses of the supersymmetric particles, for example neutralino or squark mass, can be found using edge search on the invariant mass distributions of decay products [21]. If you look at the upper decay branch on the Figure 2.4, where $\chi_2^0 \rightarrow \tilde{e}_L^- \, e^+$, you will see an example of such an edge search possibility. Knowing two final electrons

we can perform an edge search on their invariant mass to find the mass of χ_2^0. If jet can be somehow included, we can make a search for the corresponding squark mass as well. The ability to perform this analysis require more statistics and, hence, more luminosity.

REFERENCES

[1] H. Yukawa, Proc. Phys. Math. Soc. Jap. **17**, 48 (1935).

[2] E. Fermi, Z. Phys. **88**, 161 (1934).

[3] J. S. Schwinger, "Quantum electrodynamics. I: A covariant formulation," Phys. Rev. **74**, 1439 (1948).

[4] R. P. Feynman, "A relativistic cut-off for classical electrodynamics," Phys. Rev. **74**, 939 (1948).

[5] S. Weinberg, "Physical Processes In A Convergent Theory Of The Weak And Electromagnetic Interactions," Phys. Rev. Lett. **27**, 1688 (1971).

[6] P. W. Higgs, Phys. Rev. **145**, 1156 (1966).

[7] C. Burgess, G. Moore. *The Standard Model: A Primer. Cambridge University Press, 2007.*

[8] F. Halsen, A.D. Martin. *Quarks Leptons: An Introductory Course in Modern Particle Physics. John Wiley and Sons Inc., 1984.*

[9] B. Andersson et al., *Parton Fragmentation and String Dynamics,* . Rep. 97(2 3), 31-145 (1983).

[10] N. J. Cornish, D. N. Spergel, G. D. Starkman and E. Komatsu, Phys. Rev. Lett. **92**, 201302 (2004) [arXiv:astro-ph/0310233].

[11] K. A. Olive, G. Steigman and T. P. Walker, Phys. Rept. **333**, 389 (2000) [arXiv:astro-ph/9905320].

[12] M. Battaglia, I. Hinchliffe and D. Tovey, J. Phys. G **30**, R217 (2004) [arXiv:hep-ph/0406147].

[13] S. Dimopoulos and H. Georgi, "Softly Broken Supersymmetry And SU(5)," Nucl. Phys. B **193**, 150 (1981).

[14] S. Dimopoulos, S. Raby and F. Wilczek, "Supersymmetry And The Scale Of Unification," Phys. Rev. D **24**, 1681 (1981).

[15] S.P. Martin. *A Supersymmetry Primer. hep-ph/97-9356, June 2006.*

[16] I. Aitchison. *Supersymmetry in Particle Physics. Cambridge University Press, 2007.*

[17] P. Fayet and J. Iliopoulos, "Spontaneously Broken Supergauge Symmetries and Goldstone Spinors," Phys. Lett. B **51**, 461 (1974).

[18] L. O'Raifeartaigh, "Spontaneous Symmetry Breaking For Chiral Scalar Superfields," Nucl. Phys. B **96**, 331 (1975).

[19] T. Sjostrand, S. Mrenna, P. Skands   *PYTHIA Physics and Manual*   hep-ph/0603175

[20] ATLAS Collaboration. *LHC Design Report.*

[21] ATLAS Collaboration. *ATLAS detector and physics performance. Technical Design Report.* CERN/LHCC 99-14, 1999.

[22] ATLAS Collaboration. *The ATLAS Experiment at the CERN Large Hadron Collider.* JINST 3 (2008) S08003.

[23] ATLAS Collaboration. *Expected Performance of the ATLAS Experiment, Detector, Trigger and Physics.* CERN-OPEN-2008-020, Geneva, 2008.

[24] ATLAS Collaboration. *EM calorimeter calibration and performance.* CSC-EG-6, 2008.

[25] ATLAS LARG Unit. *Liquid Argon Calorimeter Technical Design Report.* CERN/LHCC 96-41, 1996.

[26] BNL group. *FECT proposal.* $http : //larg - fect.usatlas.bnl.gov/fect_docs/fct - proposal.pdf$.

[27] F. Lanni, J. McDonald, R. Stroynowski, J. Ye, P. Zarzhitsky   *Liquid argon calorimeter calibration results from Front End Crate Test.* SMU-HEP-04-08

[28] E.G. Stern W.E Cleland. *Signal processing considerations for liquid ionization calorimeters in a high rate enviroment.* Nucl. Instr. and Meth. **A 338** (1994) p. 467-497

[29] http://backreaction.blogspot.com/2007/12/running-coupling-constants.html

102

[30] H. Baer, F.E. Paige, S.D. Protopopescu, X. Tata *ISAJET 7.78*
http://www.hep.fsu.edu/ isajet/

[31] *HERWIG 6.5 An event generator for Hadron Emission Reactions With Interfering Gluons*
http://webber.home.cern.ch/webber/hw65$_m$*anual.htmlnote*1

[32] *GEANT detector description and simulation tool.*
http://wwwinfo.cern.ch/asdoc/pdfdir/geant.pdf

[33] *ATLAS Trigger Working Group web page*
https://twiki.cern.ch/twiki/bin/view/Atlas/TapmMainPage